applied sciences

MDPI

Article

Evaluation of Fracture Effectiveness in Ultra-Deep Marine Carbonate Reservoirs of Fuman Oilfield, Tarim Basin

Zedong Liu [1], Kongyou Wu [1,*], Bifeng Wang [1,*], Hui Zhang [2], Ke Xu [2] and Kehao Wang [1]

[1] School of Geosciences, China University of Petroleum (East China), Qingdao 266580, China; b22010009@s.upc.edu.cn (Z.L.); s24010041@s.upc.edu.cn (K.W.)
[2] Research Institute of Exploration and Development, Tarim Oilfield Company, PetroChina, Korla 841000, China; zhh-tlm@petrochina.com.cn (H.Z.); xuke-tlm@petrochina.com.cn (K.X.)
* Correspondence: wukongyou@163.com (K.W.); wangbifeng@upc.edu.cn (B.W.)

Abstract

Strike-slip faults and their associated fractures in the ultra-deep marine carbonate reservoirs of the Fuman Oilfield, Tarim Basin, hold significant petroleum geological importance, with the developmental characteristics of fractures being a key factor controlling reservoir productivity. This study targets the F_I17 strike-slip fault zone within the oilfield, where a comprehensive evaluation of fracture effectiveness was performed by integrating geological methods, including core and thin section observation, fluid inclusion thermometry, geophysical fracture identification approaches using imaging logging and seismic data, and geomechanical simulations. The results showed that: (1) structural fractures were developed in at least three stages, predominantly high-angle fractures with their strikes obliquely intersecting the main fault at a small angle, and were affected by multiple episodes of fluid activity, while early-phase fractures exhibited severe filling whereas late-phase fractures had good effectiveness; (2) ultra-deep carbonate rocks contained well-developed stylolites, with extensive horizontal stylolites reducing fracture effectiveness; (3) mechanical effectiveness evaluation parameters were proposed by integrating normal stress, shear stress, and formation pressure, with slip tendency as the dominant indicator, and referenced to the leakage factor and dilation tendency to characterize fracture effectiveness; (4) dynamic effectiveness was assessed using closure/opening pressures, defining a reasonable formation pressure range for hydrocarbon exploitation. The findings of this study can provide theoretical guidance for the further exploration and development of ultra-deep reservoirs in the Fuman Oilfield.

Keywords: Fuman Oilfield; marine carbonate rocks; F_I17 strike-slip fault zone; natural fracture; fracture filling characteristics; in situ stress; fracture effectiveness

Check for updates

Academic Editor: Nikolaos Koukouzas

Received: 21 January 2026
Revised: 20 February 2026
Accepted: 22 February 2026
Published: 5 March 2026

Copyright: © 2026 by the authors. Licensee MDPI, Basel, Switzerland. This article is an open access article distributed under the terms and conditions of the Creative Commons Attribution (CC BY) license.

1. Introduction

Different from international practices, China refers to reservoirs with a burial depth greater than 6000 m as ultra-deep reservoirs [1]. The Ordovician ultra-deep marine carbonate rocks in the Tarim Basin, China, have proven to be rich in oil and gas resources. However, due to the extremely large burial depth, intense compaction, and diagenetic cementation have made the rocks very tight [2], with the matrix showing low porosity and low permeability characteristics. The unique geological setting of the Tarim Basin has led to the development of numerous intracratonic strike-slip faults with small displacement. Under the modification of strike-slip faults, the tight marine carbonate rocks have improved

their porosity and permeability, and a number of oil and gas reservoirs distributed along the faults have been developed [3]. Fractures play an important role here, as they can provide the necessary reservoir space and seepage channels for fluids [4]. Research on reservoir fractures mainly focuses on their types, genetic evolution, development characteristics, distribution laws, effectiveness, and connectivity [5–12]. Not all natural fractures are effective in their natural state. Some fractures cannot provide effective flow paths for fluids due to severe filling or closure caused by intense stress compression; these are referred to as ineffective fractures. They hinder the connectivity of the fracture network and serve as a key limiting factor for productivity in ultra-deep oil and gas exploitation. Previous research methods for fracture effectiveness have mainly focused on two aspects [13–15]: first, the intuitive characterization of fracture parameters such as filling characteristics, aperture, and petrophysical properties through outcrops, cores, thin sections, and sample experimental analyses; and second, the interpretation of fracture effectiveness parameters using logging data, seismic data, in situ stress data, well testing, and production performance data.

Some preliminary explorations have been conducted on fracture effectiveness in the Tarim Basin. Early studies mainly focused on fractures in ultra-deep tight sandstone reservoirs within the Keshen foreland thrust belt. These include effectiveness evaluations based on fracture filling and aperture [14], geomechanical assessments of fracture effectiveness [9,15], as well as comprehensive evaluations integrating structure, diagenesis, and in situ stress [16]. With the continuous advancement of exploration, the exploration and development targets of the basin have shifted to ultra-deep marine carbonate rocks controlled by strike-slip faults, yet relevant work in fracture research is still in its infancy at present. Existing achievements include the determination of fracture effectiveness based on the included the evaluation of fracture activity and its influence on seepage using geomechanics [17], and the control of tectonic diagenesis over fracture filling [18]. However, systematic research on fracture effectiveness remains lacking for the ultra-deep marine carbonate reservoirs in the Fuman Oilfield of the Tarim Basin. Early research focused more on the qualitative description of fracture characteristics, and with the extensive application of geomechanics in the study of ultra-deep reservoirs in the Tarim Basin in recent years, the geomechanical response of fractures has been mentioned as an application of in situ stress research. Nevertheless, the geomechanical evaluation parameters for fracture effectiveness are still relatively limited at present, and further exploration of the mechanical effectiveness parameters of fractures is lacking. In addition, stylolites are a common structure in carbonate reservoirs, and existing studies have indicated that their development characteristics exert an influence on the seepage capacity of carbonate reservoirs [19]. The role of stylolites has often been neglected in previous analyses of fracture effectiveness.

Based on the aforementioned problems encountered in the research on fracture effectiveness and the practical demands of hydrocarbon production in the Fuman Oilfield, this paper selected the F_I17 strike-slip fault zone in the Fuman Oilfield as the research object. Taking core, thin section, imaging logging, seismic and other data as the foundation, combined with geomechanical analysis, a comprehensive evaluation of fracture effectiveness in the F_I17 strike-slip fault zone was carried out. On the basis of previous studies on fracture effectiveness, this paper also incorporated stylolites as a consideration factor, adopted a variety of mechanical effectiveness evaluation parameters for fractures, and introduced fracture opening and closure pressures into the effectiveness evaluation system. This study aimed to provide innovative references for relevant research on fracture effectiveness of ultra-deep carbonate reservoirs and offer support for the further hydrocarbon production in the Fuman Oilfield.

2. Geological Setting

The Tarim Basin is located in the southern part of Xinjiang Uygur Autonomous Region, China. It is a typical large-scale cratonic depression basin and currently China's largest marine carbonate petroliferous basin [3]. The study area, the Fuman Oilfield, is situated in the Aman Transition Zone in the middle of the Northern Depression of the Tarim Basin. Stretching north–south between the two major paleo-uplifts (the Tabei Uplift and the Central Uplift), the Aman Transition Zone dips eastward and westward into the Manjiaer Sag and Awat Sag, forming a "saddle-shaped" transition zone (Figure 1). The research object of this study is the F_I17 strike-slip fault zone, a large oil- and gas-rich fault zone within the Fuman Oilfield, with an extension length of nearly 70 km in the oilfield area. The evolution of this fault zone has experienced at least three stages: the Middle Caledonian, Late Caledonian, and Middle-Late Hercynian [20]. The Paleozoic strata in the Fuman Oilfield are well-developed. Affected by multi-stage tectonic movements, the strike-slip fault can vertically cut through multiple sets of Paleozoic strata, connecting the hydrocarbon source rocks of the Yurtus Formation (Cambrian) downward and modifying the marine carbonate reservoirs of the Yijianfang Formation and Yingshan Formation (Ordovician) upward. Meanwhile, under the seal of the thick mudstones of the Santamu Formation (Ordovician), a complete "source-reservoir-caprock" assemblage can be formed [21].

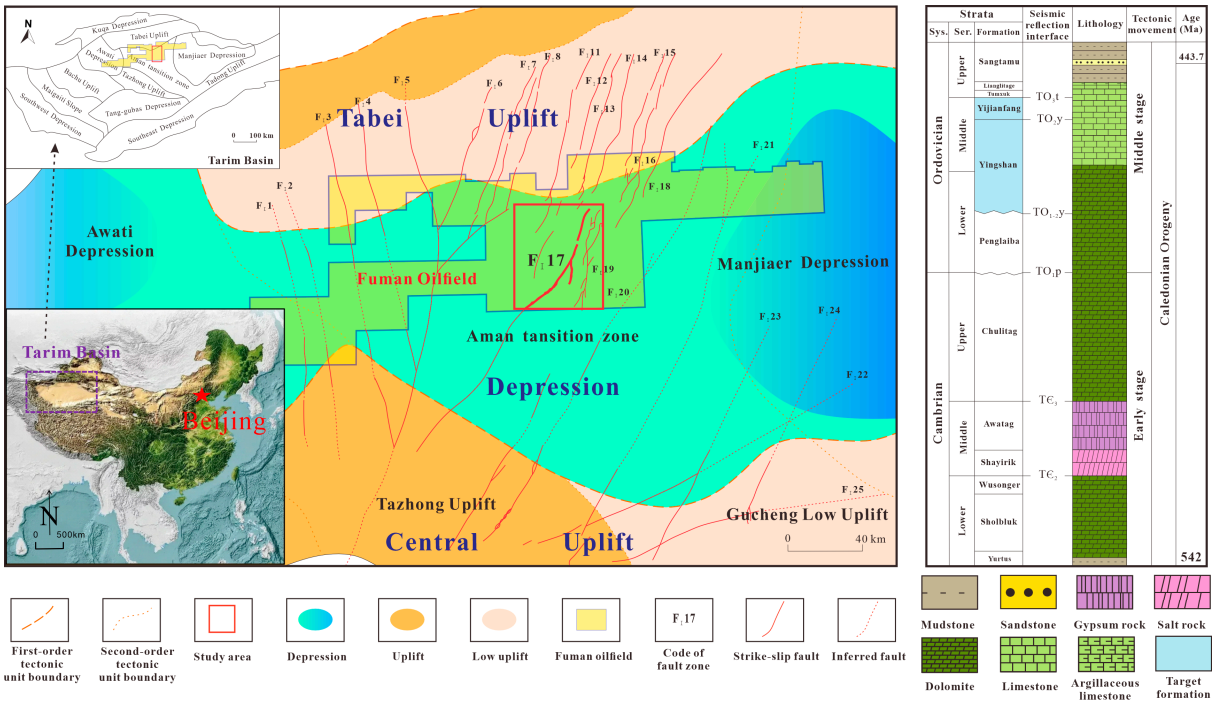


Figure 1. Map of the study area and brief overview of Paleozoic stratigraphy.

The main target layers for development in the Fuman Oilfield are the Yijianfang Formation and the top of the Yingshan Formation (Ordovician). The lithology consists of grain limestone deposited in open platform facies gravel shoals and micritic limestone deposited in inter-shoal sea environments [22], with an overall burial depth ranging from 6500 m to 8500 m. All discovered high-yield oil and gas reservoirs in the area are distributed along strike-slip faults, belonging to fault-controlled fracture-vug reservoirs [23,24]. In 2020, Well W1 deployed along the F_I17 strike-slip fault zone achieved a major oil and gas breakthrough [25], confirming the great potential of this fault zone for ultra-deep fault-controlled fracture-vug reservoirs. With the advancement of oil and gas geological research on the F_I17 strike-slip fault zone, scholars have found differences between the

fault-controlled fracture-vug reservoirs in the Fuman area (especially represented by the F_I17 strike-slip fault zone) and those developed on the peripheral uplifts of the Fuman area in the early stage [26]. In the peripheral uplift areas, the reservoirs are mainly formed by the dissolution and modification of marine carbonate rocks by meteoric fresh water on the basis of fractures and faults, forming a complex karst fracture-vug system that provides huge reservoir space for oil and gas. However, drilling core data from the F_I17 strike-slip fault zone have confirmed that the dissolution effect of meteoric fresh water is very weak, showing the basic characteristic of "more fractures and fewer vugs". This makes the contribution of fractures to oil and gas reservoirs more prominent, and the research on fracture effectiveness has become a key issue urgently needing clarification in the study area.

3. Methods and Parameters

The effectiveness of reservoir fractures is a key factor for evaluating their contribution to reservoirs. Among them, filling property and aperture are the two primary parameters characterizing fracture effectiveness [27]. The main factors affecting these two parameters include, on the one hand, fluid activities during geological history—fracture filling characteristics can be evaluated through cores, thin sections, logging data. On the other hand, geomechanical factors are also a critical link influencing fracture effectiveness; the coupling relationship between in situ stress, formation pore pressure, and fractures can dynamically affect fracture aperture and even fracture opening and closing. The dynamic evaluation of fracture effectiveness is also more suitable for the needs of current oil and gas development. Therefore, based on drilling coring, this study first observed the macroscopic fracture characteristics and conducted sampling. Subsequently, a comprehensive analysis was performed using multiple methods, including microscopic observation, fluid inclusion homogenization temperature measurement, and whole-rock geochemical analysis, as well as numerical simulation of the stress field (Figure 2). Meanwhile, to better support the numerical simulation of the stress field and the study on fracture response to stress variations, high-temperature and high-pressure triaxial compression tests and fracture stress sensitivity experiments were also carried out. Through the above technical workflow, the evaluation of fracture effectiveness in ultra-deep marine carbonate reservoirs was accomplished.

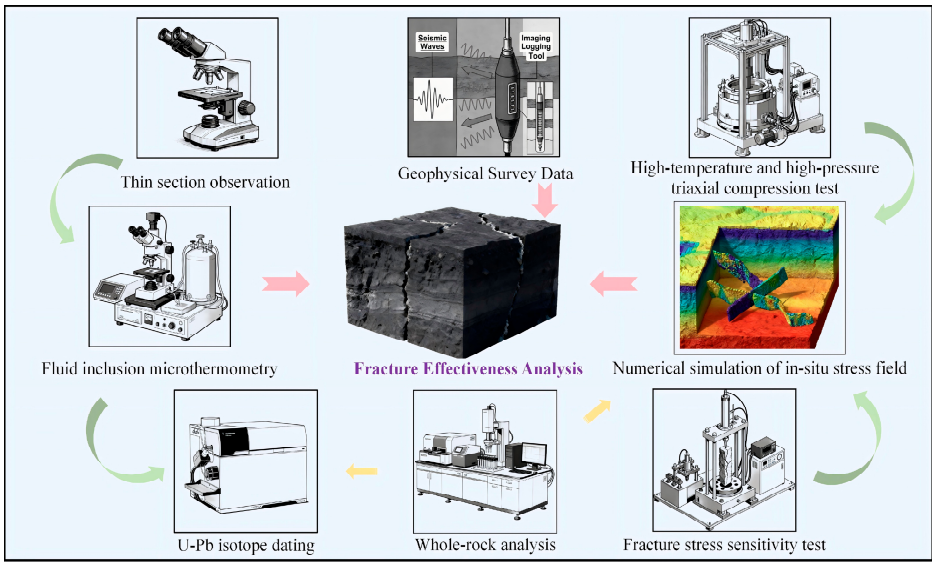


Figure 2. Research methods for fracture effectiveness.

3.1. Geological Observation, Geochemical and Geophysical Methods

We conducted observations on 11 core wells in the Fuman Oilfield, including five wells within the F_I17 strike-slip fault zone, with a cumulative core observation length of over 150 m; more than 30 samples were collected, yielding 19 core plugs and a number of thin sections (Figure 3). Preliminary observations of fracture characteristics (e.g., type, sets, filling, aperture, density, and hydrocarbon-bearing property) were performed on cores. Selected samples were then processed into thin sections, which were observed under an optical microscope to determine fracture phases, fillings, and fluid inclusion types. Using a heating-freezing stage, the homogenization temperatures of fluid inclusions in the thin sections (Figure 4a) were measured, and the timing of fluid activity was constrained by U-Pb isotope dating data. Based on the thermal and burial history of the reservoir, we analyzed the evolutionary sequence of fracture effectiveness and its impact on hydrocarbon reservoirs. Integrating geological observations, geochemical analyses, and imaging logging data (Figure 4b), we clarified the differences and connections between fracture development and filling characteristics at different scales. Finally, via fracture identification using likelihood seismic attributes (Figure 4c), we established a full-sequence description of fracture characteristics spanning microscale (under microscope), mesoscale (logging), and macroscale (seismic) scales.

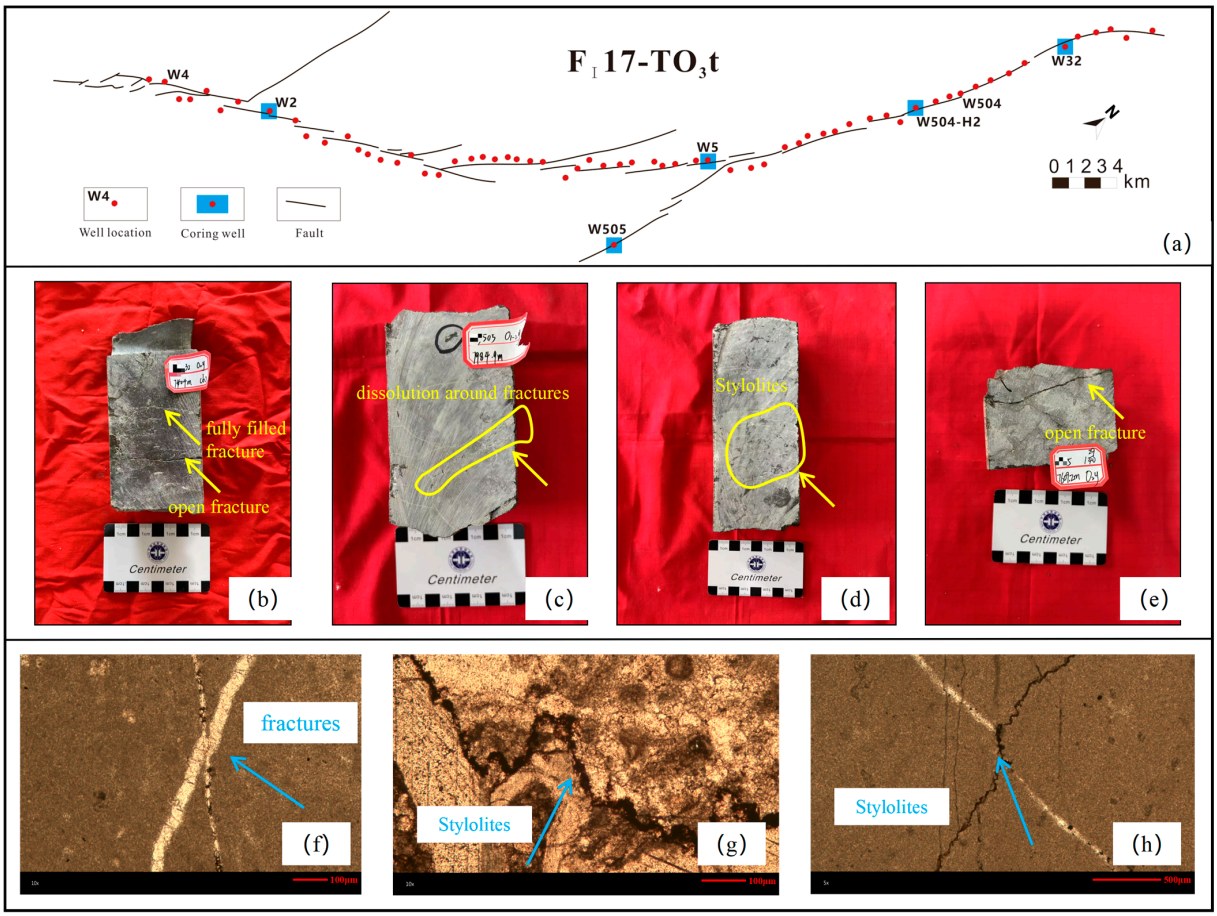


Figure 3. (**a**) F_I17 strike-slip fault zone and well location distribution. (**b**) Fully filled fractures and open fractures, Well W32, 7404 m, O_2y. (**c**) Dissolution around fractures, Well W505, 7984.9 m, $O_{1-2}y$. (**d**) Stylolites, Well W505, 8077.3 m, $O_{1-2}y$. (**e**) Open fractures, Well W5, 7609.2 m, O_2y. (**f**) Intersection of two sets of fractures (under microscopic observation), Well W505, 7983 m. (**g**) Bitumen-filled stylolites (under microscopic observation), Well W5, 7609 m. (**h**) Stylolites cutting through early fractures (under microscopic observation), Well W2, 7788 m.

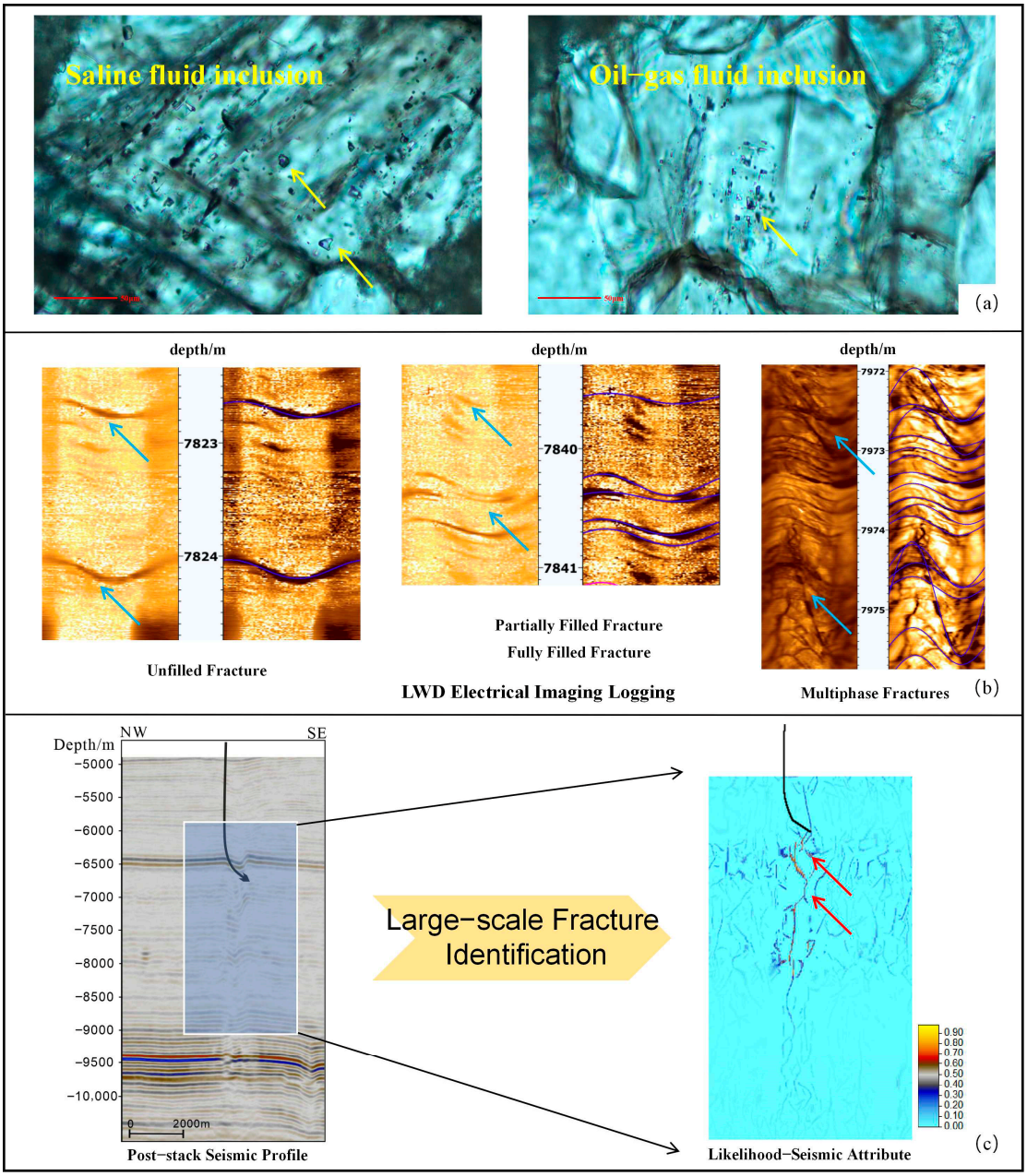


Figure 4. (**a**) Microscopic photographs of inclusions (Well W5, 7609 m, O_2y). (**b**) Typical imaging logging images of fractures. (**c**) Large−scale fracture identification based on seismic attributes.

Through core and thin section observations, a large number of stylolites have been identified in marine carbonate rock, and there are generally complex cross-cutting relationships between stylolites and fractures. In previous studies on fracture effectiveness, the role of stylolites has rarely been mentioned. However, actual observations have shown that stylolite development can, on the one hand, promote dissolution, while on the other hand, fully filled tight stylolites can also act as fluid barriers. The widespread presence of tight stylolites can block fluid seepage in multi-scale fractures. Therefore, in this study, several stylolites were observed from cores and under a microscope to summarize their characteristics (such as type and filling property), thereby analyzing the significance of these characteristics for fracture effectiveness.

3.2. Geomechanical Method

To support the study of fracture effectiveness from a geomechanical perspective, this study has also conducted high-temperature and high-pressure triaxial compression tests and fracture stress sensitivity tests to investigate the static mechanical parameters of rocks and the stress response laws of fractures, respectively. To simulate the characteristics of "high geothermal temperature and high stress" in the ultra-deep environment, the triaxial compression tests were carried out under conditions of 150 °C and 140 MPa confining pressure.

In the experimental methods, the intrinsic properties of fractures (such as aperture, density, and filling property) can be qualitatively and semi-quantitatively evaluated by means of microscopic observations. Traditional analyses have suggested that fractures with larger aperture, higher density, and poorer filling property tend to have better effectiveness. However, combined with production practice, it has been found that not all fractures conform to this basic understanding—fractures with excellent intrinsic effectiveness are often not ideal reservoir spaces and seepage channels. This mainly depends on extrinsic factors, such as environmental factors including in situ stress. Previous studies have confirmed that the coupling relationship between in situ stress, fractures, and pore fluids can directly control fracture effectiveness [9].

In this study, data from imaging logging were used to conduct single-well one-dimensional (1D) stress simulation for analyzing the effectiveness of fractures around the wellbore. The selection of these wells with imaging logging data for single-well evaluation was mainly due to three reasons: (1) the direction of horizontal principal stresses can be determined based on the characteristics of drilling-induced fractures and borehole collapse observed in imaging logging images; (2) imaging logging data can interpret the development characteristics of meter-scale fractures around the wellbore, bridging the excessive scale gap between fracture observation under a microscope and identification via seismic data; and (3) imaging logging data can finely characterize fracture effectiveness parameters, which can fully verify and supplement the results of qualitative and semi-quantitative evaluations in experiments. In addition, this study also employed the finite element method (FEM) to perform three-dimensional (3D) in situ stress simulation. Meanwhile, combined with seismic attribute extraction, large-scale fractures were identified, and their stress states were analyzed to investigate their effectiveness under the current stress condition. In the process of stress field numerical simulation, various parameters are involved, and the methods for acquiring and calculating these parameters are introduced below.

3.2.1. Rock Mechanics Parameters

The most fundamental rock mechanics parameters required for in situ stress calculation are Young's modulus and Poisson's ratio. Dynamic parameter calculations can be performed by leveraging the correlation between mechanical parameters and acoustic wave velocity. Subsequently, combined with the calibration of results from high-temperature and high-pressure triaxial compression tests (Figure 5), the dynamic rock mechanics parameters are converted into static mechanical parameters.

$$\mu_d = \frac{0.5(v_p/v_s)^2 - 1}{(v_p/v_s)^2 - 1} = \frac{v_p^2 - 2v_s^2}{2\left(v_p^2 - v_s^2\right)} = \frac{\Delta t_s^2 - 2\Delta t_p^2}{2\left(\Delta t_s^2 - \Delta t_p^2\right)} \quad (1)$$

$$E_d = 10^6 \frac{\rho v_s^2 \left[3\left(v_p/v_s\right)^2 - 4\right]}{\left(v_p/v_s\right)^2 - 1} = 10^6 \frac{\rho v_s^2 \left(3v_p^2 - 4v_s^2\right)}{v_p^2 - v_s^2} = 10^6 \frac{\rho\left(3\Delta t_s^2 - 4\Delta t_p^2\right)}{\Delta t_s^2\left(\Delta t_s^2 - \Delta t_p^2\right)} \quad (2)$$

where v_s is the shear wave velocity (m/μs); Δt_s is the shear wave interval transit time (μs/m); v_p is the compressional wave velocity (m/μs); Δt_p is the compressional wave

interval transit time (μs/m); ρ is the rock density (g/cm^3); μ_d is the dynamic Poisson's ratio; and E_d is the dynamic elastic modulus (GPa).

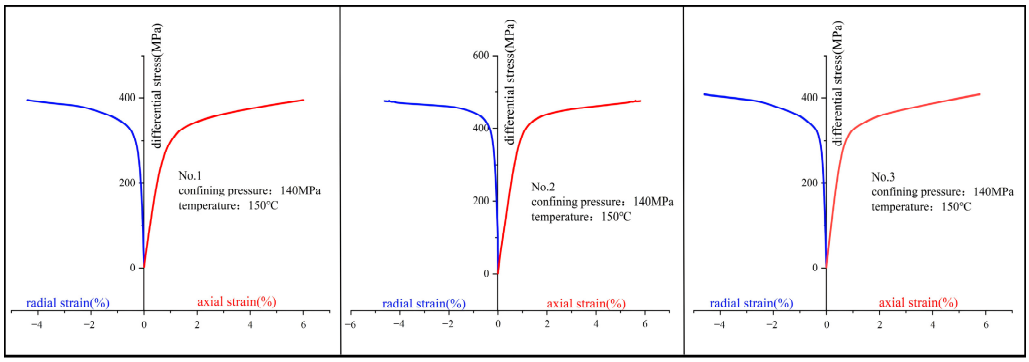


Figure 5. Stress–strain curves of rock triaxial compression tests.

By performing a univariate linear fitting between the dynamic parameters calculated from logging data and the static parameters obtained from experiments, an empirical formula for dynamic–static parameter conversion can be derived. In this paper, combined with the results of this triaxial compression test and the previous practical data in the study area, the following formula was adopted for the conversion of dynamic and static parameters.

$$\mu_s = 0.3608\mu_d + 0.1454 \tag{3}$$

$$E_s = 0.6146E_d - 4.6505 \tag{4}$$

where E_s is the static elastic modulus (GPa); E_d is the dynamic elastic modulus (GPa); μ_s is the static Poisson's ratio; and μ_d is the dynamic Poisson's ratio.

3.2.2. Formation Pore Pressure

Common methods for calculating formation pore pressure include the equivalent depth method, Bowers method, effective stress method, and Eaton method. Among these, the Eaton method is the most widely applied. However, the underdevelopment of mudstones in marine carbonate formations can limit the applicability of the Eaton method, which is more suited for sand-shale sequences. Therefore, the Bowers method was adopted in this study [28,29].

$$p_p = \sigma_v - \left(\frac{v_p - 1500}{A}\right)^{\frac{1}{B}} \tag{5}$$

where p_p is the formation pore pressure (MPa); σ_v is the vertical stress (MPa); v_p is the compressional wave velocity (m/s); and A and B are regional empirical parameters.

3.2.3. Direction of Horizontal Principal Stress

The direction of horizontal principal stress can be derived from imaging logging data (Figure 6). The principal stress direction can be indicated by identifying borehole breakouts and drilling-induced fractures, and its principle can be elaborated based on the analysis of borehole stress states. In the direction of the minimum principal stress, the tangential normal stress reaches its maximum value, where stress collapse is prone to occur and form elliptical boreholes. This phenomenon is referred to as borehole breakout, and the major axis of the elliptical borehole indicates the direction of the minimum horizontal principal stress. In the direction of the maximum horizontal principal stress, the tangential normal stress is minimized. When the drilling fluid pressure is relatively high, tensile stress is generated on the borehole wall surface in this direction, which tends to induce

drilling-induced fractures; the strike of these fractures can indicate the direction of the maximum horizontal principal stress.

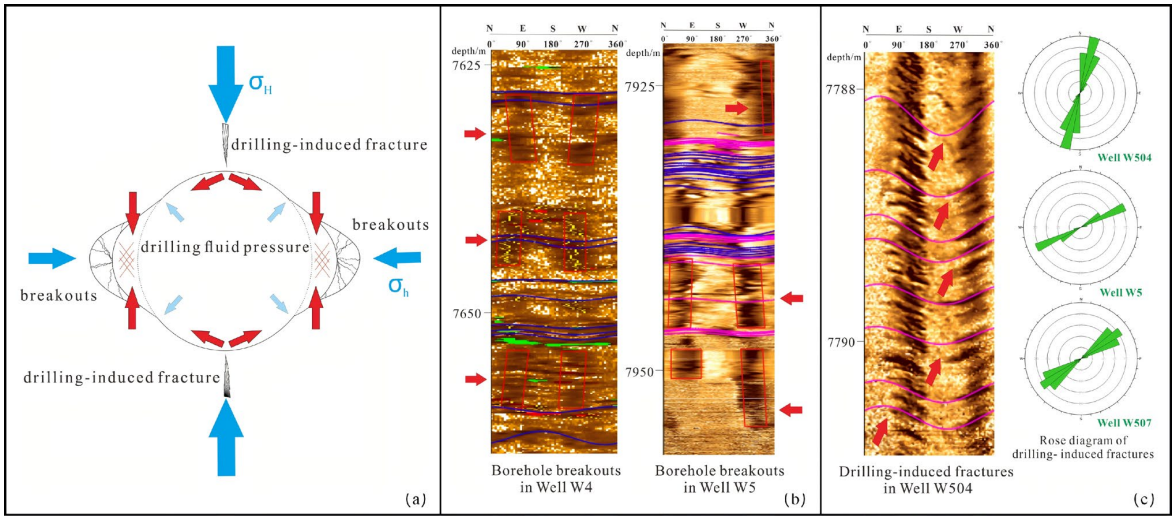


Figure 6. Signature map of horizontal principal stress direction identification around borehole by imaging logging. (**a**) Identification markers for principal stress direction via imaging logging. (**b**) Borehole breakouts. (**c**) Drilling-induced fractures.

3.2.4. In Situ Stress Calculation Model

Numerous models have been proposed for one-dimensional (1D) horizontal in situ stress calculation in wellbores, such as the uniaxial strain model, Huang's model, Mohr–Coulomb model, composite spring model, and poroelastic medium model. Verified by exploration and development practices, the composite spring model yields favorable application results in the study area [16]. The composite spring model is derived from the generalized Hooke's law, based on the assumptions that rocks are homogeneous and isotropic linear elastic materials, there is no relative displacement between formations during sedimentation and subsequent tectonic movements, and the strains in the two horizontal directions of formations remain constant. This model can comprehensively consider the influences of formation rock mechanical properties, pore pressure, and tectonic activities on in situ stress. The calculation results of 1D wellbore in situ stress can be used as a reference for loading boundary conditions of the three-dimensional (3D) finite element model, and can also serve as a validation for the 3D finite element simulation results. The formula for calculating in situ stress is as follows [9,20]:

$$\sigma_v = \int_0^{H_0} \rho_0(h) g dh + \int_{H_0}^{H} \rho(h) g dh \tag{6}$$

$$\sigma_h = \frac{\mu}{1-\mu}(\sigma_v - \alpha p_p) + \frac{E\xi_{\mathrm{h}}}{1-\mu^2} + \frac{\mu E \xi_H}{1-\mu^2} + \alpha p_p \tag{7}$$

$$\sigma_H = \frac{\mu}{1-\mu}(\sigma_v - \alpha p_p) + \frac{E\xi_H}{1-\mu^2} + \frac{\mu E \xi_{\mathrm{h}}}{1-\mu^2} + \alpha p_p \tag{8}$$

where σ_V is the vertical stress (MPa); H_0 is the depth of the logging starting point (m); $\rho_0(h)$ is the density at depth h in the non-logged interval (g/cm^3); $\rho(h)$ is the logging density at depth h (g/cm^3); g is the gravitational acceleration (m/s^2); σ_H is the maximum horizontal principal stress (MPa); σ_h is the minimum horizontal principal stress (MPa); μ is Poisson's ratio; E is Young's modulus (GPa); ξ_H and ξ_h are the tectonic strain coefficients along the directions of the maximum principal stress and minimum principal stress; α is the Biot coefficient; and p_p is the formation pore pressure (MPa).

The establishment of the 3D in situ stress model was mainly based on the Petrel platform. The 3D reservoir geological model of the F_I17 strike-slip fault zone was constructed using three structural horizons: TO_3t (top surface of the Yijianfang Formation), TO_2y (bottom surface of the Yijianfang Formation), and $TO_{1-2}y$ (bottom surface of the Yingshan Formation). After considering geological accuracy and computational efficiency (with the number of grids as far as possible less than 10 million), a grid division scheme of 125 × 125 m in the horizontal direction and 80 layers in the vertical direction was adopted to establish the 3D geomechanical model. After assigning rock mechanical parameters and formation pore pressure, the faults and fractures of the F_I17 strike-slip fault zone were incorporated as discontinuities. Finally, with the 1D in situ stress calculation results as constraints, the maximum and minimum horizontal strain values were repeatedly adjusted.

3.2.5. Stress State of Fracture Surfaces

The stresses exerted by the current in situ stress field on natural fracture surfaces can be decomposed into the normal stress σ_n perpendicular to the fracture surfaces and the shear stress τ parallel to the fracture surfaces (Figure 7). The coupling between these two stresses and formation pore pressure can affect the opening, closing and sliding behaviors of natural fractures, thereby controlling the seepage characteristics of fractures. The normal stress and shear stress can be obtained by decomposing and synthesizing the stresses on fracture surfaces based on the stress simulation results [30].

$$\sigma_n = \sigma_v \cos^2\theta + \sigma_H \sin^2\theta \sin^2\beta + \sigma_h \sin^2\theta \cos^2\beta \quad (9)$$

$$\tau = \sqrt{\sigma_v^2 \cos^2\theta + \sigma_H^2 \sin^2\theta \sin^2\beta + \sigma_h^2 \sin^2\theta \cos^2\beta - \sigma_n^2} \quad (10)$$

where σ_v is the vertical stress (MPa); σ_H is the maximum horizontal principal stress (MPa); σ_h is the minimum horizontal principal stress (MPa); θ is the fracture dip angle (°); β is the acute angle between the fracture strike and the maximum horizontal principal stress (°); σ_n is the normal stress (MPa); and τ is the shear stress (MPa).

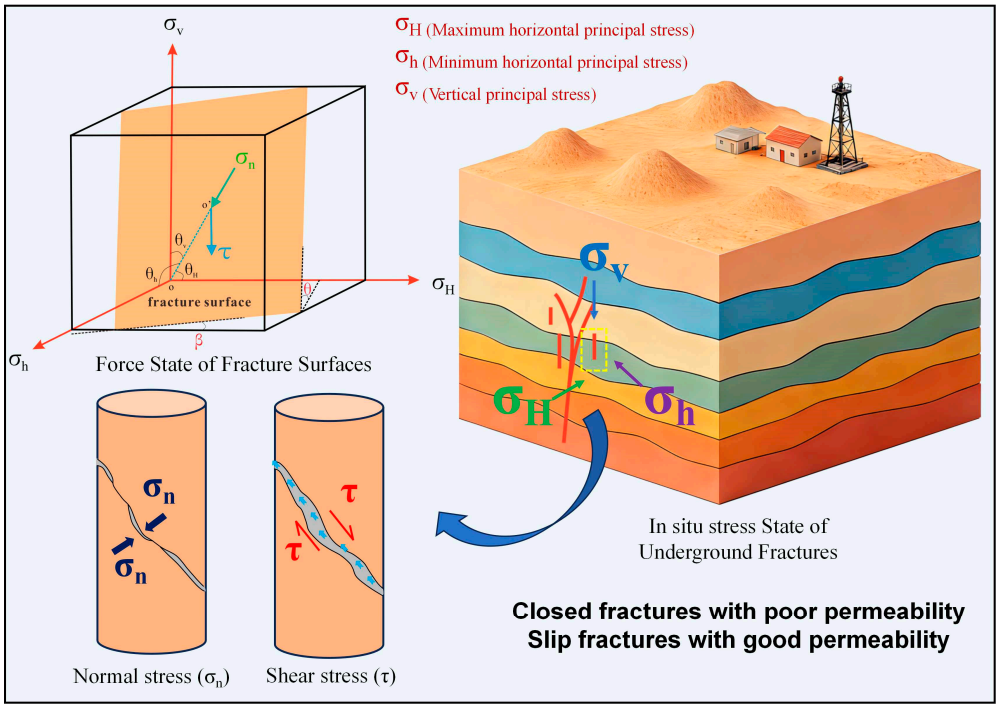


Figure 7. Mechanism map of fracture effectiveness controlled by normal and shear stresses.

3.3. Mechanical Evaluation Parameters for Fracture Effectiveness

In ultra-deep reservoirs, the mechanical state of fractures is regarded as one of the key factors affecting fracture effectiveness, referred to as fracture mechanical effectiveness for short. Under the current in situ stress, fractures in a critical sliding state exhibit favorable seepage capacity [31,32]. Among relevant parameters, the ratio of shear stress to effective normal stress, τ/σ_{ne} (where effective normal stress is defined as the normal stress minus formation pore pressure), was recognized as a robust parameter to characterize the sliding state of such structural planes. This ratio was named the slip tendency coefficient [33], which can serve as an important index reflecting fracture permeability and fluid flow behavior.

$$T_s = \frac{\tau}{\sigma_{ne}} \tag{11}$$

where T_s is the slip tendency coefficient; τ is the shear stress (MPa); and σ_{ne} is the effective normal stress (MPa).

Byerlee et al. (1978) obtained through friction experiments that the friction coefficient (ratio of shear stress to normal stress) of rocks ranges from 0.6 to 1 [34]. Zoback concluded that fractures with a friction coefficient lower than 0.6 on the fracture surface were not permeable, and 0.6 was also regarded as the threshold value for the critical sliding state [35]. That is, when the slip tendency coefficient exceeded the critical friction coefficient of 0.6, the fractures were considered to undergo shear sliding, which will activate the originally impermeable fractures. The Mohr's circle can intuitively represent the stress state of any plane in space, and it is an effective tool for analyzing the stress characteristics on fracture surfaces, which can assist us in evaluating the mechanical effectiveness of fractures. It is worth noting that the mechanical effectiveness of fractures is not merely a static parameter, but an index with dynamic changes. As can be seen from the Mohr's circle, with the variation in formation pore pressure, the Mohr's circle may shift leftward or rightward, and the number of effective fractures above the Mohr–Coulomb failure line also changes. That is, the mechanical effectiveness of some fractures can transform between effective and ineffective states (Figure 8). Of course, practical engineering has also confirmed that the critical threshold may be lower than 0.6, which can depend on the inherent strength of the fractures themselves.

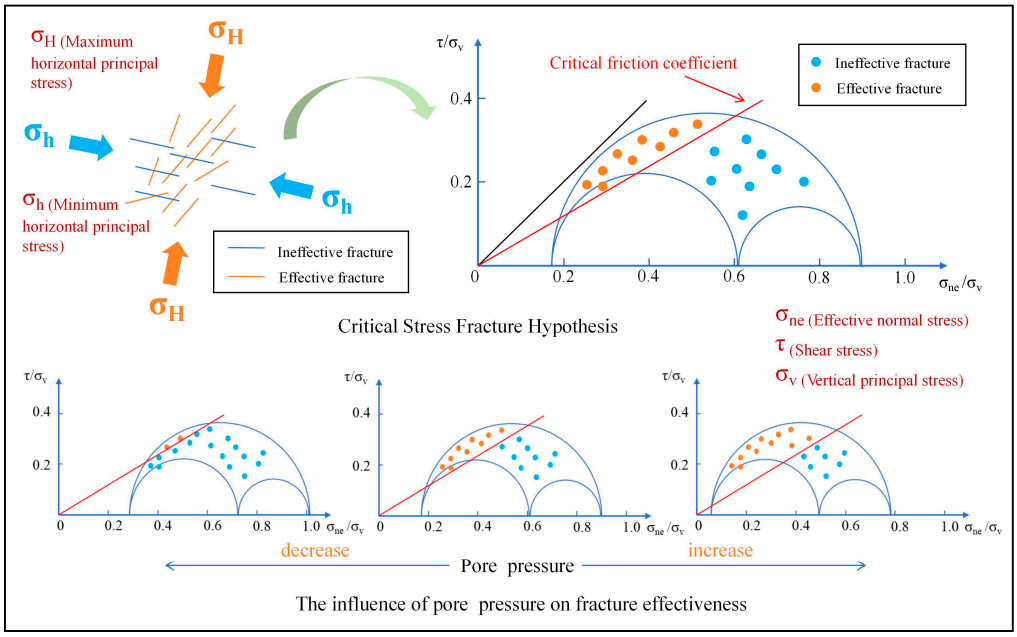


Figure 8. Analysis of fracture mechanical effectiveness based on Mohr's circle.

The essence of the shear-to-normal stress ratio parameter lies in the coupling relationship among normal stress, shear stress, and pore pressure. Based on the correlations between these three factors, this study further proposed two additional parameters for evaluating the mechanical effectiveness of fractures, namely the dilation tendency coefficient T_d and the leakage factor T_l [36].

$$T_d = (\sigma_1 - \sigma n)/(\sigma_1 - \sigma_3) \tag{12}$$

$$T_l = p_p/(\sigma_n - \tau) \tag{13}$$

where T_d is the dilation tendency coefficient; T_l is the leakage factor; σ_1 is the maximum principal stress (MPa); σ_3 is the minimum principal stress (MPa); p_p is the formation pore pressure (MPa); τ is the shear stress (MPa); and σ_n is the normal stress (MPa).

During the development of oil and gas reservoirs, initial depletion-driven production led to a continuous decline in formation pressure. As observed from the Mohr's circle, a decrease in formation pressure will cause more fractures to close and transition from an effective state to an ineffective one. Ineffective fractures can no longer serve as pathways for oil and gas migration, resulting in poor fluid flow, production decline, or even production shutdown. In the subsequent secondary development stage, energy supplementation measures such as water/gas injection were adopted, allowing formation pressure to recover. With the restoration of formation pressure, fractures re-opened and reverted from an ineffective state to an effective state. However, some fractures with high sliding tendency may induce water channeling after opening, which impaired the efficiency of secondary development.

Meanwhile, to more intuitively evaluate the changes in fracture states induced by reservoir development and precisely define the reasonable range of formation pressure for production, researchers commonly took formation pressure as a reference and calculate the fracture opening pressure and closing pressure to guide reservoir development [37,38]. The open and closed states of fractures can also be used to characterize the dynamic changes in fracture mechanical effectiveness.

The opening pressure of fractures was affected by multiple factors, including fracture properties, occurrence, in situ stress distribution, and pore pressure. Its calculation formula is as follows [37]:

$$P_o = \frac{\mu}{1-\mu}\sigma_v \sin\theta + \sigma_v \cos\theta - p_p + \sigma_H \sin\theta \sin\beta + \sigma_h \sin\theta \cos\beta \tag{14}$$

where P_o is the fracture opening pressure (MPa); μ is Poisson's ratio; σ_v, σ_H and σ_h are the vertical stress, maximum horizontal principal stress and minimum horizontal principal stress, respectively (MPa); p_p is the formation pore pressure (MPa); θ is the fracture dip angle (°); and β is the acute angle between the fracture strike and the maximum horizontal principal stress (°).

Previous studies derived the calculation formula for the closure pressure of fractures in carbonate reservoirs using the Zienkiewicz–Pande failure criterion [38]:

$$P_f = \sigma_n - \frac{\sqrt{N^2 - 4MK} - N}{2M} \tag{15}$$

$$M = \frac{4}{3}\frac{\sin^2\phi_0}{(3-\sin\phi_0)^2}\left(\frac{1+\mu}{1-\mu}\right)^2 + \left(\frac{2\mu-1}{1-\mu}\right)\left(\frac{36 - 34\sin\phi_0 \sin^2 3\theta_\sigma - 4\sin^2\phi_0 \sin^2 3\theta_\sigma}{96 + 12\cos^2\phi_0}\right) \tag{16}$$

$$N = \frac{8c\sin\phi_0\cos\phi_0}{(3-\sin\phi_0)^2} \tag{17}$$

$$K = \frac{12c^2 \cos^2 \phi_0 (1 - 576 \tan\phi_0)}{576 \tan\phi_0 (3 - \sin \phi_0)^2} \quad (18)$$

where P_f is the fracture closing pressure (MPa); σ_n is the normal stress (MPa); ϕ_0 is the internal friction angle (°); μ is Poisson's ratio; c is the cohesion (MPa); and θ_σ is the stress Lode angle (°).

4. Results

4.1. Static Evaluation of Fracture Effectiveness Characteristics

A statistical analysis was conducted on the fracture filling characteristics of cores from five cored wells in the F_I17 strike-slip fault zone. The results showed that fully filled fractures accounted for 52%, partially filled fractures for 19%, and unfilled fractures for 29%, with fractures possessing certain seepage capacity making up 48% of the total. However, one core sample from Well W505 was excluded from the statistics (Figure 3d). This exclusion was primarily due to the abnormally developed fractures in this core—21 fully filled fractures were densely distributed within a sample length of approximately 20 cm, with a density far higher than that of other core samples. Combined observations of cores and microscopic analysis revealed that the fractures exhibited characteristics of at least three phases (Figure 9a), with later-formed fractures cutting through earlier-formed ones being visible. Unfilled fractures (Figure 9b) and stylolite structures, which are common in marine carbonate rocks, as shown in (Figure 9c), were also observed in the cores. The stylolites could be classified into two types based on their amplitude variation patterns: one type was low-amplitude stylolites, mostly occurring at low angles to the bedding planes, and the other type was steeply inclined to the bedding planes with drastic amplitude variations. Microscopic observations indicated that the fractures were mainly filled with calcite, dolomite, and bitumen (Figure 9d–f), showing a filling sequence of more than three phases in the following order: calcite → dolomite → bitumen.

Based on the imaging logging data from five wells in the F_I17 strike-slip fault zone, a total of 595 structural fractures were identified, predominantly striking NE–SW (Figure 10a), which was approximately consistent with the strike of the main fault. Statistical analysis of fracture dip angles (Figure 10b) showed that high-angle and near-vertical shear fractures dominated overall: high-angle oblique fractures (45–75°) accounted for 45.21%, and vertical fractures (75–90°) accounted for 54.29%, with a combined proportion of 99.5%. The effectiveness of fractures with different dip angles varied in ultra-deep layers, where under extreme overburden pressure high-angle fractures generally exhibited better effectiveness than low-angle ones. Thus, the widely developed high-angle to near-vertical fractures provided a favorable hydrocarbon migration and accumulation foundation for the F_I17 strike-slip fault zone. Meanwhile, fracture filling characteristics can be observed from the image features of resistivity imaging logs. Structural fractures typically appeared as sinusoidal curves: bright sinusoids indicate fractures filled with high-resistance minerals such as calcite, while dark sinusoids resulted from the invasion of high-conductivity drilling mud into unfilled or partially filled fractures. Statistical results of fracture characteristics from imaging logs showed that unfilled fractures (with the best effectiveness) accounted for 55.3%, partially filled fractures (with moderate effectiveness) for 23.7%, and fully filled (ineffective) fractures for 21% (Figure 10c). This indicated that most fractures can serve as fluid storage spaces and seepage channels. Notably, fracture filling characteristics derived from imaging logs differed from the statistics from core samples. This discrepancy may arise from the low core recovery rate in intervals with well-developed unfilled open fractures during ultra-deep drilling, leading to an overrepresentation of filled fractures in

the retrieved cores. In contrast, imaging logging data may more closely reflect the actual fracture conditions.

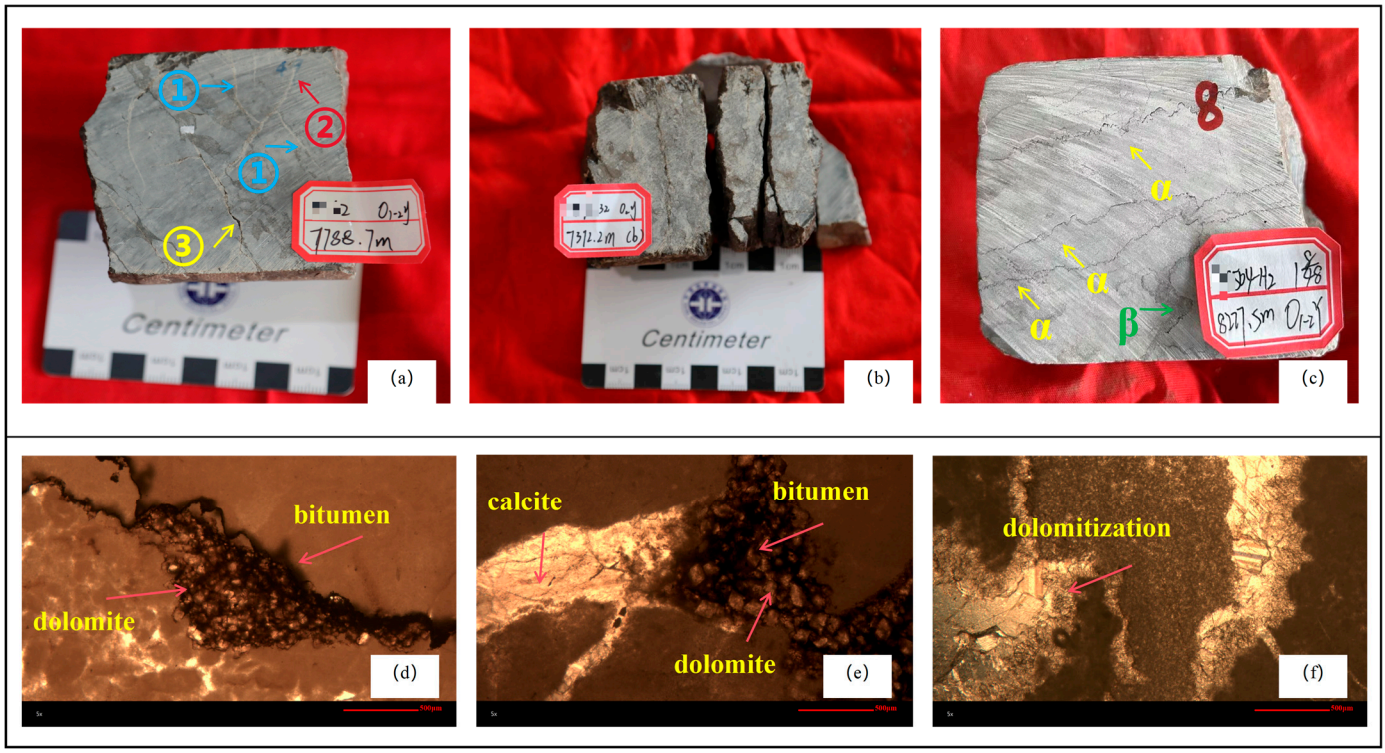


Figure 9. (**a**) Polyphase fractures (①, ②, ③), Well W2, 7787.7 m, $O_{1-2}y$. (**b**) Unfilled fractures, Well W32, 7372.2 m, O_2y. (**c**) Two types of stylolites (α, β), Well W504-H2, 8227.5 m, $O_{1-2}y$. (**d**) Dolomite- and bitumen-filled stylolites, Well W2, 7784.6 m, $O_{1-2}y$. (**e**) Multi-stage filled fractures, Well FY3-H2 (F_I16 strike-slip fault zone), 7626.5 m, $O_{1-2}y$. (**f**) Dolomitization, Well W504-H2, 8230.2 m.

In addition to the occurrence and filling characteristics of the aforementioned fractures affecting their effectiveness, the coupling relationship between fracture occurrence and in situ stress was also an important influencing factor. Imaging logging results from multiple wells showed that fracture dip angles were relatively consistent, but strike characteristics were not obvious and appeared relatively discrete. Considering the strike variation in the F_I17 strike-slip fault zone, the strikes of its associated fractures also exhibited certain differences along the fault zone. Therefore, the fracture strikes in the imaging logs of five wells were statistically analyzed separately (Figure 10d). Among them, the fractures in Wells W2, W32, and W504 were mainly NNE-SSW striking, while those in Wells W4 and W5 were predominantly NEE-SWW striking, generally obliquely intersecting the main fault direction at a small angle. The width differences in fractures with different filling characteristics can be directly observed in imaging logs (Figure 10c): unfilled effective fractures had the largest width, followed by partially filled ones, and fully filled fractures had the smallest width. Most fracture apertures ranged from 0.5 to 2.5 mm. Although this did not represent the true underground fracture aperture, considering that high-angle fractures accounted for the majority of the total number, the apparent aperture observed in imaging logs can also reflect the relative size of the aperture to a certain extent.

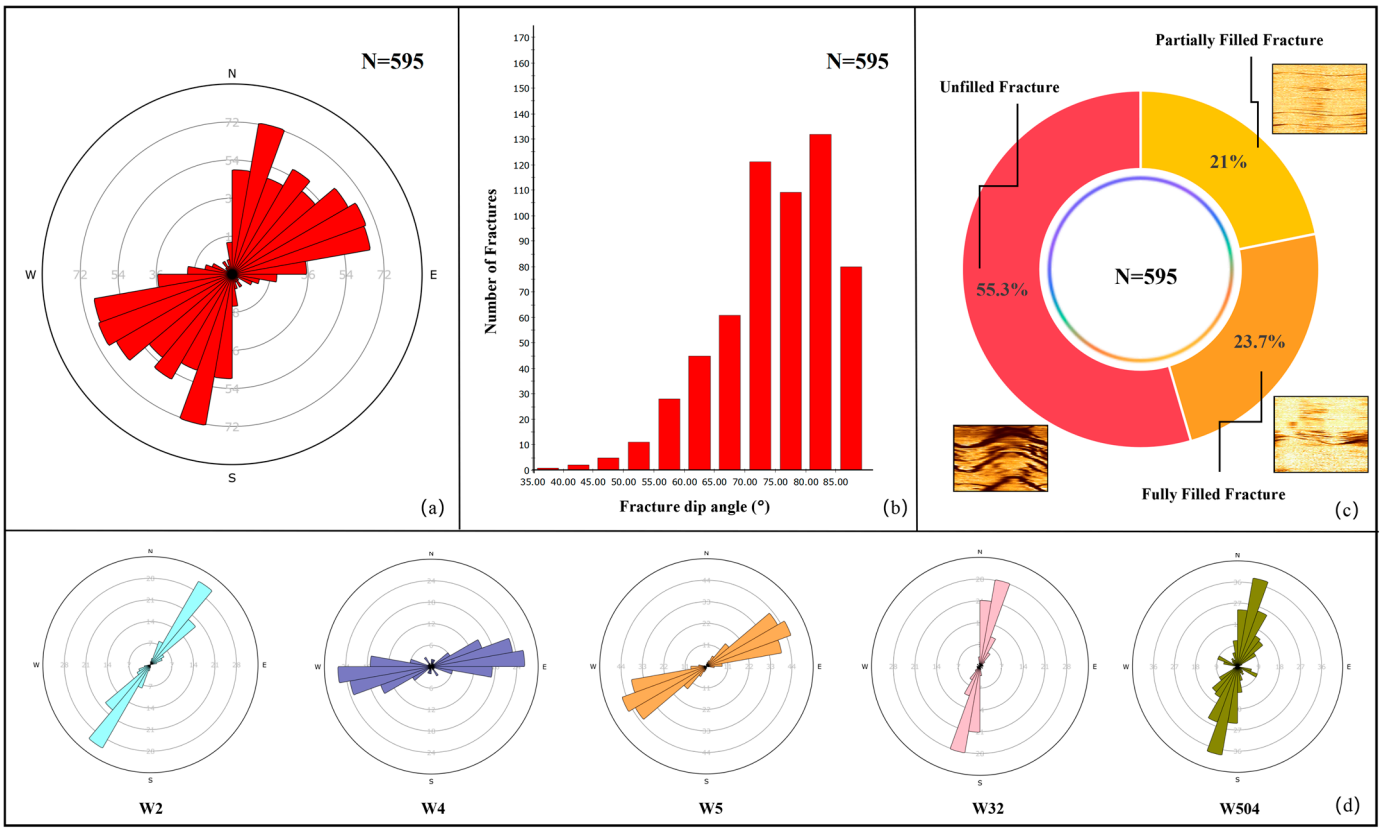


Figure 10. Statistics of fracture parameters from imaging logging (data from wells: W32, W2, W4, W5, and W504). (**a**) Rose diagram of fracture strike. (**b**) Dip angle distribution of fractures. (**c**) Statistics of fracture filling characteristics. (**d**) Rose diagram of fracture strike for single well. (Where different colors denote different wells.).

Under microscope observation, most cements in reservoir fractures were calcite, and the developed fluid inclusions were mainly aqueous inclusions and hydrocarbon inclusions. The inclusions exhibited diverse morphologies, including elliptical, square, and irregular shapes, with significant differences in size where the long axis ranged from 3 to 7 μm. Homogenization temperatures of fluid inclusions from Wells W32, W2, and W504-H2 were measured using a heating–freezing stage, with a total of 50 fluid inclusions tested (Figure 11a), including 16 from Well W32, eight from Well W2, and 26 from Well W504-H2. A small number of hydrocarbon inclusions had relatively low homogenization temperatures (<70 °C). Excluding hydrocarbon inclusions, the stages of diagenetic cementation in fractures can be preliminarily determined based on the peak intervals of homogenization temperatures of aqueous inclusions. For Well W32, the homogenization temperatures of aqueous inclusions ranged from 81.5 to 116.6 °C (Figure 11b). From the temperature distribution, the fractures had undergone at least three stages of cementation, with main peak intervals at 80–90 °C (average 85.5 °C), 100–110 °C (average 105.5 °C), and 110–120 °C (average 115 °C). For Well W504-H2, the homogenization temperatures ranged from 81.5 to 142.7 °C (Figure 11c), indicating 3–4 stages of cementation, with main peak intervals at 70–80 °C (average 76.7 °C), 80–90 °C (average 85.5 °C), 100–110 °C (average 105.4 °C), and 110–120 °C (average 115.2 °C). For Well W2, the homogenization temperatures of aqueous inclusions ranged from 84.9 to 123.8 °C (Figure 11d), showing three stages of cementation, with main peak intervals at 80–90 °C (average 85.1 °C), 100–110 °C (average 106.6 °C), and 120–130 °C (average 122.7 °C).

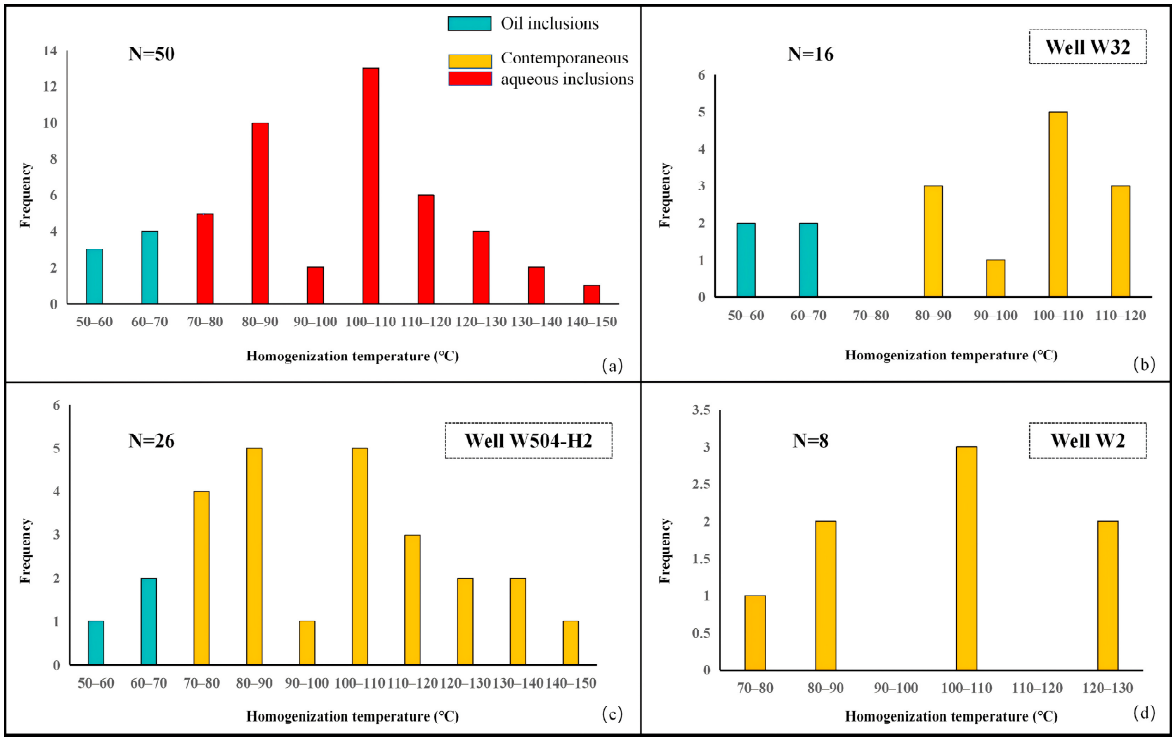


Figure 11. Fluid inclusion thermometry of the F_I17 strike-slip fault zone. (**a**) Total homogenization temperature distribution. (**b**) Homogenization temperature distribution of Well W32. (**c**) Homogenization temperature distribution of Well W504-H2. (**d**) Homogenization temperature distribution of Well W2.

Comprehensive analysis of the homogenization temperature distribution of fluid inclusions from all wells (Figure 11a) indicated that the fractures in the F_I17 strike-slip fault zone had experienced at least three stages of cementation.

4.2. Current Stress State of Fractures

The results of the high-temperature and high-pressure triaxial compression tests are presented in Table 1. To clarify the source of parameter differences, one core sample each was collected from the Yijianfang Formation of Well W2 (7782.5 m) and the Yingshan Formation of Well W8 (8161.7 m) for bulk rock elemental analysis. The results indicated that the limestone of the Yingshan Formation had a relatively high dolomite content (47%), classifying it as dolomitic limestone, while the mineral composition of the Yijianfang Formation sample was dominated by calcite (97.6%).

Table 1. Results of high-temperature and high-pressure triaxial compression tests.

Sample	Well	Strata	Temperature (°C)	Confining Pressure (MPa)	Young's Modulus (GPa)	Poisson's Ratio
1	W32	O_2y	150	140	36.4	0.27
2	W504-H2	$O_{1-2}y$	150	140	44.1	0.25
3	F302-H6	$O_{1-2}y$	150	140	46.9	0.28

The results of the aforementioned triaxial compression tests can provide certain references for the establishment of mechanical materials, preventing the mechanical parameter model from deviating from the actual range. However, due to the limited number of experimental samples, the static data cannot be effectively used as constraints for constructing mechanical parameter models, and can only verify the rationality of the empirical mechani-

cal parameter model for the F_I17 strike-slip fault zone to a certain extent. Meanwhile, the stress results calculated for single wells can be used as the calibration for the 3D finite element simulation results, thereby completing the 3D simulation of the F_I17 strike-slip fault zone. It should be noted that the scarcity of ultra-deep core samples for laboratory mechanical experiments and the lack of in situ stress measurement data may introduce certain errors into the simulation results. Yet from the perspective of practical drilling applications, such errors in the study area were within an acceptable range. The results showed that (Figure 12): (1) The Young's modulus ranged from 32 to 47 GPa with an average value of 40.6 GPa, while the Poisson's ratio ranged from 0.23 to 0.26 with an average value of 0.24. In the vertical direction, the distribution of elastic parameters exhibited differences and stratification characteristics with increasing depth. The Yijianfang Formation in the shallow section had stronger planar heterogeneity, and the difference in elastic modulus of the surrounding rock decreased with increasing depth. In the planar view, affected by the fault zone, there was an obvious difference in elastic parameters between the surrounding rock and the fault. A decrease in Young's modulus (by approximately 20%) and an increase in Poisson's ratio (by approximately 10%) can be observed near the fault-developed areas. Along the fault strike, the variation in elastic parameters of the southern segment of the fault was more significant compared with the surrounding rock, while the difference in the northern segment was reduced. (2) The minimum horizontal principal stress ranges from 110 to 170 MPa and the maximum horizontal principal stress ranges from 145 to 205 MPa. In the vertical direction, both principal stresses increased with increasing depth, with the average principal stress increasing by nearly 10 MPa from the Yijianfang Formation to the Yingshan Formation. In the horizontal direction, disturbed by the F_I17 fault zone, the stress along the fault strike direction was discontinuous, and there were differences in the magnitudes of horizontal principal stresses. Spatially, the principal stress in the fault zone was in a low-value area, showing an obvious stress drop phenomenon, with the local stress drop reaching more than 15%.

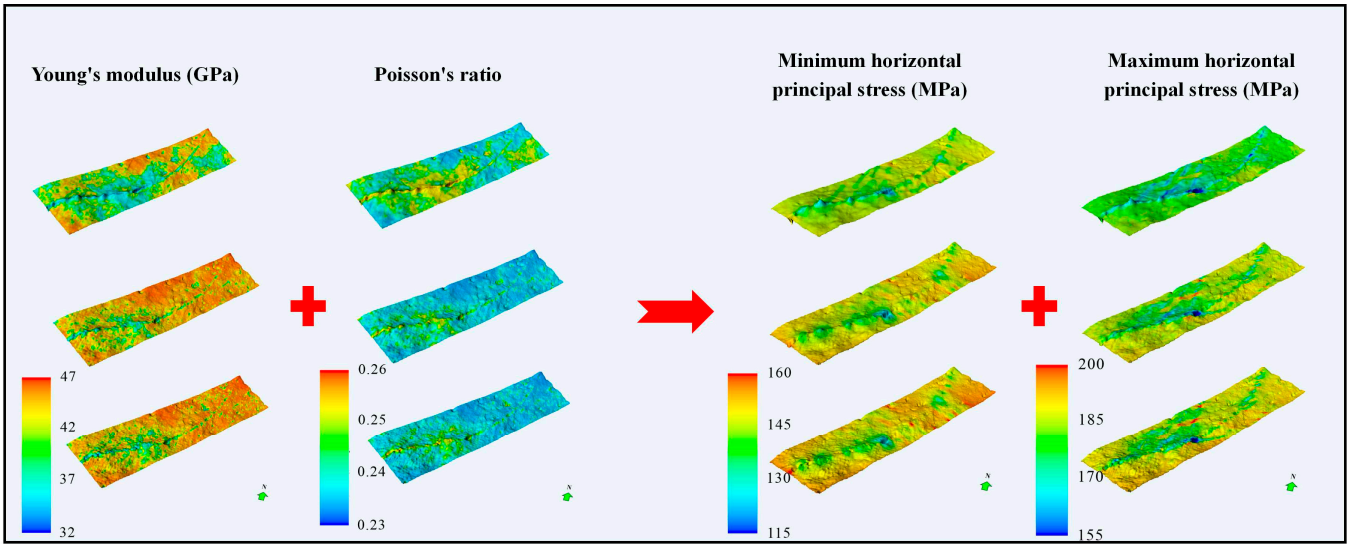


Figure 12. Results of rock mechanical parameters and stress field simulation.

Large-scale natural fractures in reservoirs can be identified based on seismic likelihood volume attributes, thereby establishing a fracture model (Figure 13). The workflow was as follows: First, perform structure-oriented filtering on the post-stack seismic data, followed by maximum likelihood calculation based on seismic data similarity. This attribute represented the probability of fault/fracture occurrence, with a value range of 0 to 1. Combined with drilling and logging data from single wells, the effective threshold of the maximum

likelihood attribute can be calibrated, which was set to 0.45 in this study. Finally, fracture modeling was conducted based on the spatial distribution of large-scale fractures delineated by the likelihood attribute, and qualified fracture planes were extracted. The 3D in situ stress simulation results were assigned to the fracture patches of the fracture model as mean values to show the stress characteristics of large-scale natural fracture surfaces. Combined with Equations (9) and (10), the normal stress and shear stress on the fracture surfaces can be solved. To better reflect the stress state on the fracture walls, the normal stress was subtracted by the pore pressure and presented as effective normal stress. For the large-scale natural fracture surfaces related to the F_I17 strike-slip fault zone, the effective normal stress ranged from 30 to 105 MPa, and the shear stress ranged from 5 to 35 MPa (Figure 13). Normal stress was generally considered the most direct factor for fracture closure, and the differences in fracture effectiveness can be intuitively observed through the relative magnitude of normal stress on the fracture surfaces.

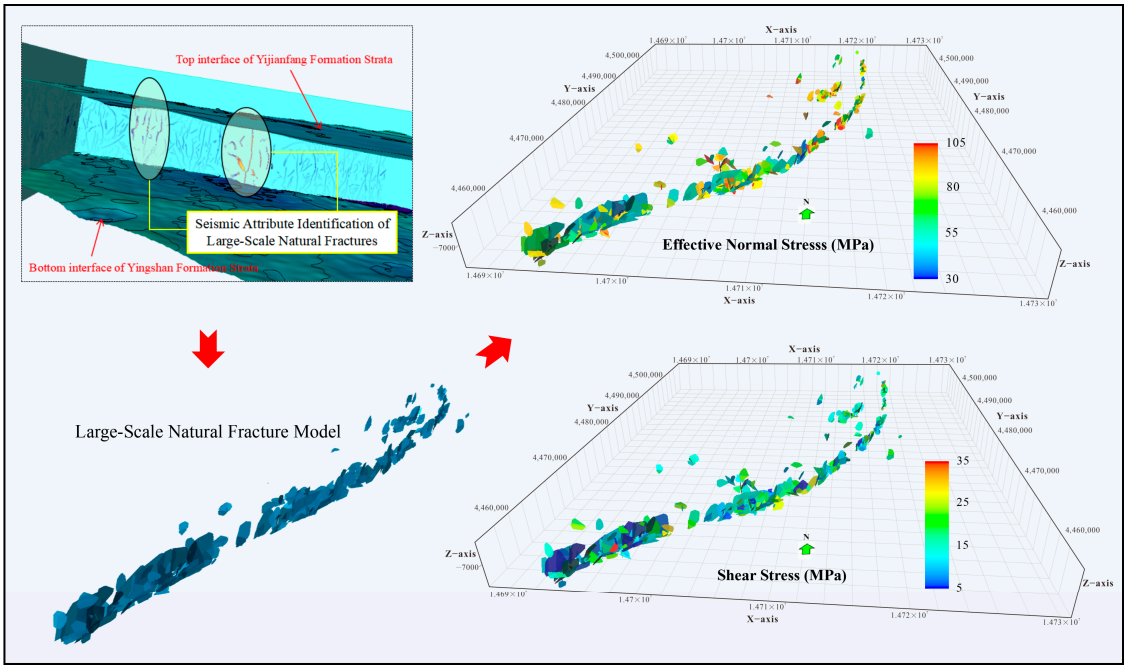


Figure 13. Stress state of large-scale natural fractures.

4.3. Mechanical Effectiveness Evaluation of Fractures

After clarifying the values of various stresses on the large-scale fracture surfaces, the mechanical effectiveness parameters of fractures can be solved separately using Equations (11)–(13) (Figure 14), thereby analyzing the mechanical effectiveness of large-scale fractures from a macroscopic perspective. Calculations showed that for the large-scale natural fractures in reservoirs related to the F_I17 strike-slip fault zone, the shear–normal stress ratio (slip tendency coefficient) ranged from 0.1 to 0.55, the dilation tendency coefficient ranges from 0.2 to 0.85, and the leakage factor ranged from 0.4 to 0.7. These parameters were the result of the coupling of in situ stress, pore pressure, and the occurrence of large-scale fractures, and can provide references for the quantitative evaluation of fracture effectiveness. Meanwhile, seismic-scale fractures were also the main seepage channels; the matching relationship between stress and fractures determined the quality of mechanical effectiveness and significantly affected their seepage capacity. During well placement in the exploration stage, locations with good mechanical effectiveness of fractures were usually selected.

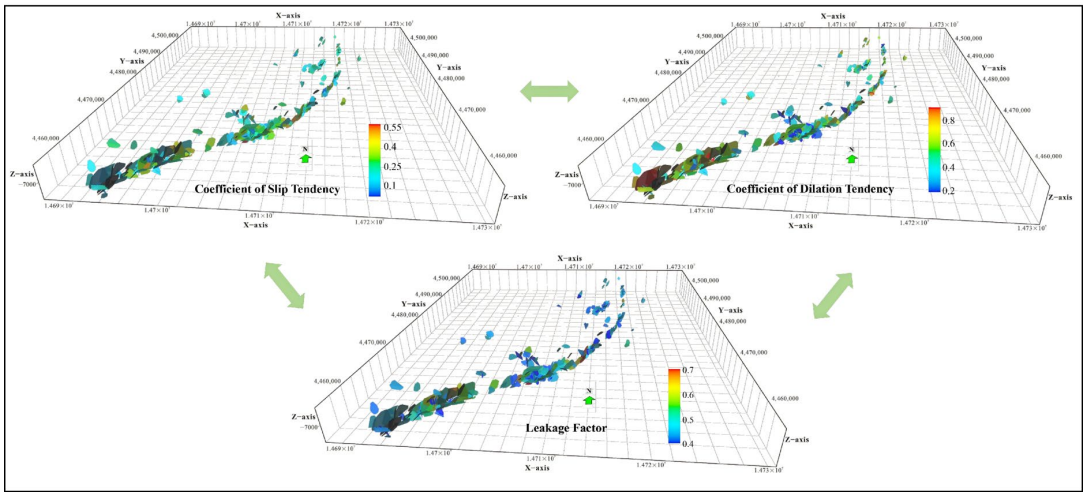


Figure 14. Mechanical parameters of fracture effectiveness.

In the development of ultra-deep reservoirs, greater attention was paid to the mechanical effectiveness of near-wellbore fractures, which affected the productivity of individual wells. The mechanical effectiveness of near-wellbore fractures can be evaluated using the aforementioned three parameters, or alternatively, the dynamic fracture effectiveness indicators characterized by Equations (14)–(18)—closure pressure and opening pressure.

A total of 595 near-wellbore fractures were identified via imaging logging in five wells of the F_I17 strike-slip fault zone. The stress conditions of near-wellbore fractures at different depths were obtained using Equations (5)–(9), and then the opening pressure and closure pressure of near-wellbore fractures were calculated via Equations (14)–(18) (Figure 15). Calculations showed that the fracture opening pressure ranged from 100 to 250 MPa, and the fracture closure pressure ranged from 20 to 70 MPa, with slight differences in pressures among different wells.

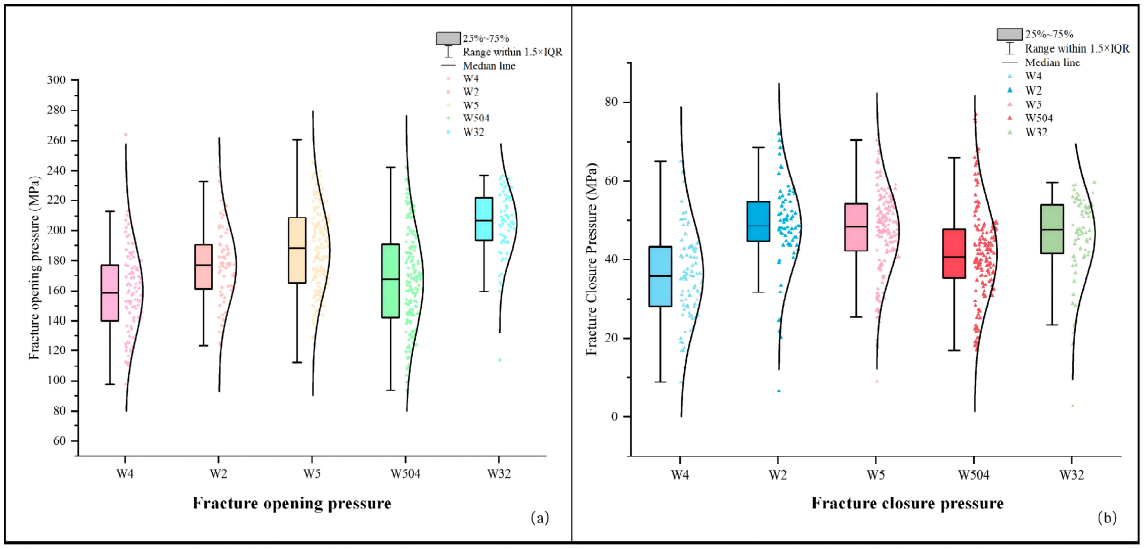


Figure 15. (**a**) Box plot of fracture opening pressure. (**b**) Box plot of fracture closure pressure. (Where different colors denote different wells.).

5. Discussion

5.1. The Influence of Fluid Activity

Fracture effectiveness is controlled by multi-stage tectonism and fluid activity. Three stages of tectonic fractures can be distinguished based on crosscutting relationships

and filling differences observed in thin sections and core samples (Figures 3f,h and 9a). Combined with the kinematic evolution history of the Fuman area, the main fracture-forming stages were the Middle Caledonian, Late Caledonian–Early Hercynian, and Late Hercynian–Indosinian [39]. The timing of fluid activities was determined using the peak ranges of fluid inclusion homogenization temperatures (Figure 11a) and U-Pb dating results (Table 2), and then matched with fracture stages to analyze fracture effectiveness (Figure 16). Combined with previous studies, four major episodes of fluid activity occurred in the study area [40]: Middle Caledonian; Late Caledonian–Early Hercynian; Late Hercynian–Indosinian; and Himalayan. Fractures formed from the Caledonian to Early Hercynian were filled with calcite under the influence of meteoric freshwater and formation water. During the Late Hercynian, fractures were affected by hydrothermal and mixed fluids, showing complex filling characteristics. Apart from calcite cementation, bitumen filling around dolomite can be observed microscopically, and hydrothermal alteration also generated minor dissolution pores near tectonic fractures (Figure 3c), which improved fracture effectiveness. Diagenetic fluid activity was weak during the Indosinian–Himalayan, but 1–2 stages of hydrocarbon charging occurred, with organic acids derived from hydrocarbon generation as the main fluid. Overall, fractures formed in the Late Hercynian–Indosinian underwent fewer episodes of fluid activity and relatively low filling degrees, thus presenting high effectiveness and acting as the main pathways for late-stage hydrocarbon charging.

Table 2. U-Pb dating data of calcite veins in the F_I17 strike-slip fault zone, Fuman area [41,42].

Sample	Well	Age (Ma)
1	W5	457 ± 13
2	W32	372.6 ± 4.6
3	W2	368 ± 3.3
4	W2	359 ± 5.6

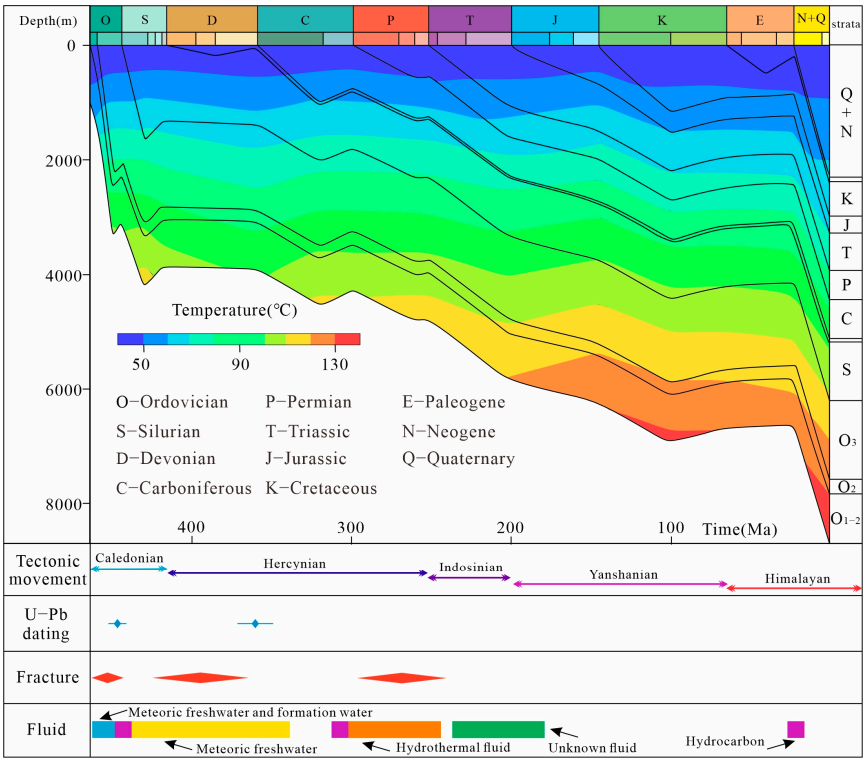


Figure 16. Matching relationship between fractures and fluid activities.

5.2. The Influence of Stylolites

In addition to tectonic fractures, stylolite structures were widely developed in the study area (Figure 3g,h and Figure 9c). According to stylolite density statistics of cored wells: W504-H2 had 22.2 stripes/m (30 in 1.35 m); W5, 17.3 stripes/m (14 in 0.81 m); W2, 10.5 stripes/m (18 in 1.71 m); W32, 6.5 stripes/m (21 in 3.23 m); and W505, the lowest at 4.3 stripes/m (9 in 2.09 m). Stylolites were highly developed within the main fault zone. A large number of bitumen fillings were observed inside these stylolites under the microscope, indicating that they were once pathways for hydrocarbon migration in the early stage and thus constituted effective fractures during the geological history. However, they were currently intensely filled, leaving almost no effective space for fluid flow. As a result, excessively developed stylolites tended to reduce the overall effectiveness of the fracture system. Two types of stylolites were identified based on morphological observations: One type was serrated stylolites parallel to the bedding planes (accounting for 77.4%). These stylolites were formed by pressure solution as a result of the long-term accumulation of overlying stress, exhibiting regular overall morphology and small amplitude fluctuations, the width ranges from 0.5 to 1.0 mm. The other type was stylolites perpendicular to the bedding planes (accounting for 22.6%), which were generated by the coupling of tectonic activities and pressure solution under intense horizontal compression. These stylolites were characterized by complex morphologies, variable widths, and large amplitude fluctuations. They had a high dip angle and did not significantly cut structural fractures laterally. As weak planes, they played a positive role in subsequent reservoir stimulation. Therefore, the density of horizontal zigzag stylolites can be introduced as a reference index into fracture effectiveness evaluation: the higher the density, the poorer the fracture effectiveness. Overall, in the F_I17 strike-slip fault zone, horizontal stylolites can cut through other fractures with the exception of late-stage incompletely filled open fractures. Consequently, most primary fractures were crosscut by stylolites, resulting in incomplete flow channels (Figure 3h) and a reduction in the overall fracture effectiveness.

5.3. Influencing Factors of Fracture Stress State

Fracture stress state is jointly controlled by fracture occurrence and in situ stress. In the F_I17 strike-slip fault zone, for large-scale fractures with high dip angles in the southern part, the effective normal stress was generally less than 65 MPa, while that for low-dip large-scale fractures can exceed 80 MPa (Figure 13). Based on the average values of the three principal stresses in the study area, the coupling relationship between fracture occurrence and stress was analyzed (Figure 17). When the fracture dip increased from 50° to 90°, the normal stress on the fracture plane decreased by approximately 18.4 MPa. When the angle between the maximum horizontal principal stress and the fracture strike increased from 5° to 30°, the normal stress increased by about 6.9 MPa. This indicated that fractures with higher dip angles and smaller angles between the maximum principal stress and fracture strike had better effectiveness. This was the main reason why high-angle fractures parallel to the present maximum principal stress direction exhibited stronger permeability. Meanwhile, shear stress showed a similar trend to normal stress with varying fracture occurrence, although its variation curve differed from that of normal stress.

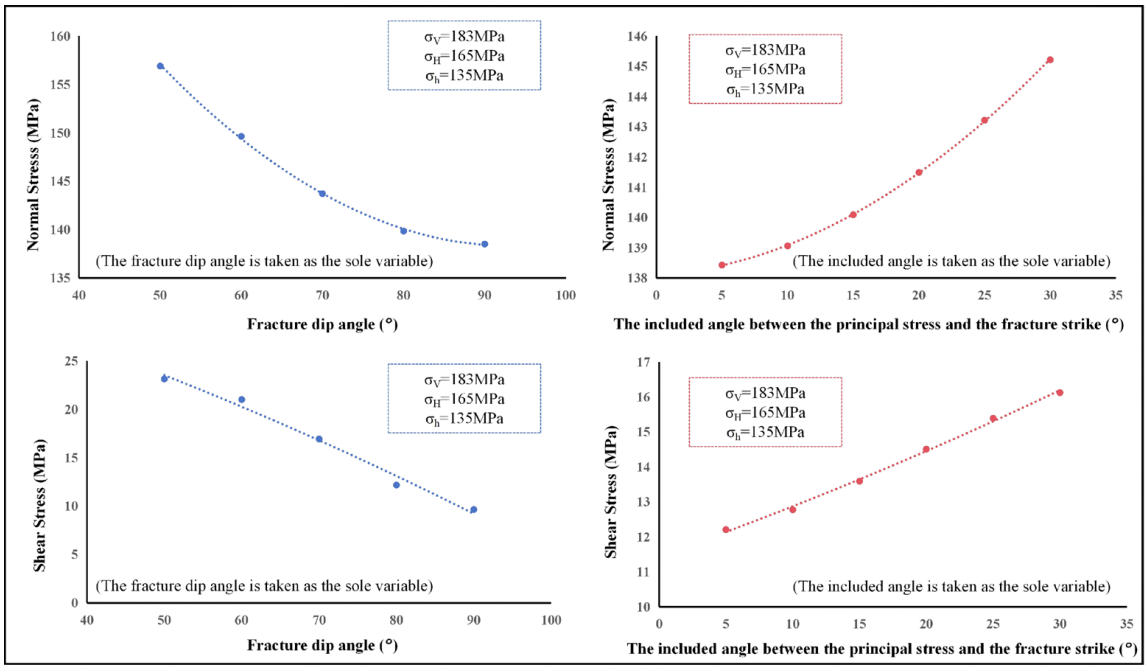


Figure 17. The influence of fracture dip angle and the angle between principal stress direction and fracture strike on normal and shear stresses.

5.4. Relationship Between Fracture Mechanical Effectiveness and Productivity

After matching the fracture mechanical effectiveness parameters (slip tendency, dilation tendency, and leakage factor) with productivity, a certain correlation was observed between each parameter and productivity (Figure 18). Given the limited volume of production data, this correlation may only be applicable to the F_I17 strike-slip fault zone. It is worth noting that the productivity data of Well W4 were excluded in this study; during drilling, significant drill drop and mud loss occurred in this well. Combined with seismic attribute calibration, it can be inferred that a large fault cavity is developed here, and its productivity was much higher than that of fracture-dominated reservoirs. The correlation analysis showed that the slip tendency coefficient has a strong positive correlation with the productivity under pressure drop, and the leakage factor also showed a positive correlation but weaker than that of the slip tendency coefficient, whereas the dilation tendency coefficient showed a negative correlation. This phenomenon indicated that the seepage contribution mechanism of fractures in ultra-deep carbonate rocks was dominated by shear dilation rather than fracture opening. In addition, fractures with a high dilation tendency coefficient may have been favorable areas for fluid and mineral precipitation during geological history [43], resulting in severe fracture cementation. The application of the slip tendency coefficient has been verified in previous practices in the Tarim Basin [9,16,17]. The numerical distribution of the leakage factor should be consistent with that of the slip tendency coefficient in principle, but it lacked clear physical significance. This factor characterized the fluid leakage, connectivity and sealing effectiveness of fractures driven by pore pressure. Its advantage could lie in being more sensitive to variations in pore pressure, making it suitable for comparing effectiveness influenced by pore pressure changes during development. Nevertheless, in terms of its correlation with productivity, its indicative significance for production was relatively limited in ultra-deep carbonate reservoirs. The dilation tendency coefficient was a parameter reflecting the potential of fracture opening and represented the capacity of fractures as fluid flow pathways. In the F_I17 strike-slip fault zone, the overall dilation tendency coefficient of fractures remained at a medium-to-high level

(T_d > 0.6), indicating that fractures were not excessively closed due to high normal stress. However, it showed an obvious negative correlation with actual productivity, which may be related to the fracture cementation in this fault zone. Therefore, in the evaluation of fracture mechanical effectiveness in the F_I17 strike-slip fault zone, the slip tendency coefficient should be taken as the dominant parameter, with the leakage factor and dilation tendency coefficient as references. Fractures characterized by high slip tendency, high leakage factor, and medium dilation tendency exhibited better productivity performance. Nevertheless, such relationships can carry a degree of uncertainty due to the limited amount of production data, particularly for the leakage factor and the dilation trend coefficient. As an exploratory attempt on mechanical effectiveness parameters, this study was meaningful, and its outcomes are expected to be fully validated, especially after the subsequent application and extension of relevant approaches in the Fuman Oilfield.

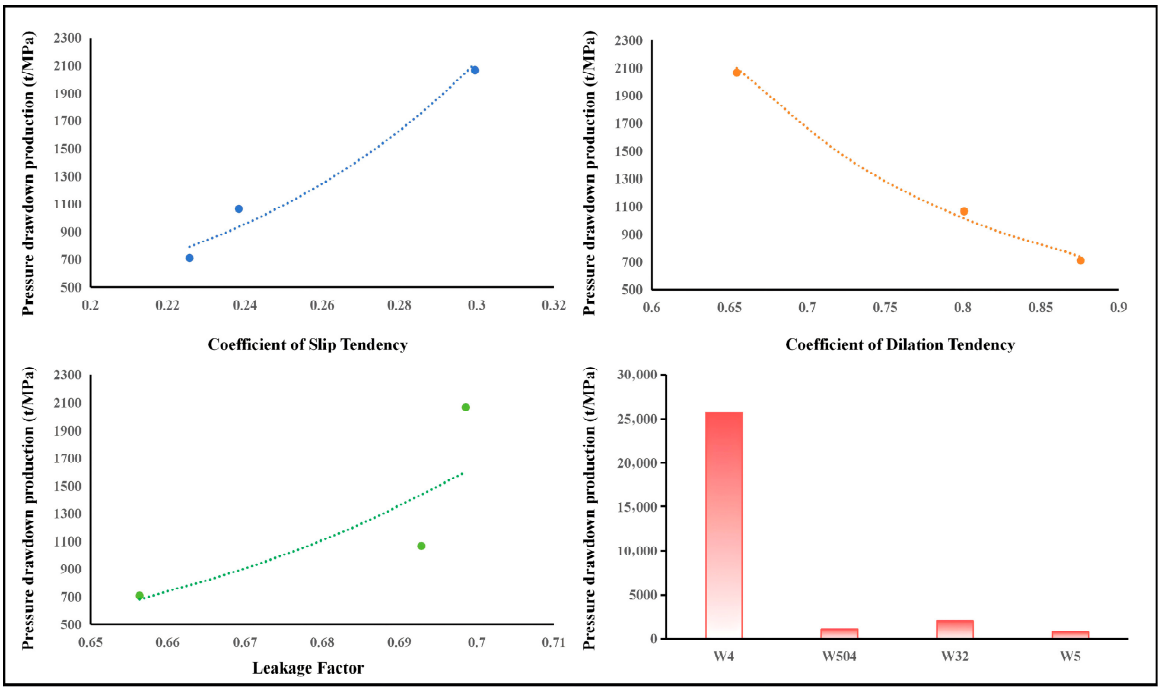


Figure 18. The relationship between slip tendency coefficient, dilation tendency coefficient, leakage factor, and pressure drop and production rate.

In addition to fracture effectiveness, the number of developed fractures also affected productivity [14]. Scatter plots of the slip tendency coefficient at the imaging logging scale were drawn at different depths for Wells W32, W5, and W504 (Figure 19). It can be seen that Well W32, with higher productivity, has the fewest fractures (73), but the highest slip tendency coefficient, generally greater than 0.2. For Wells W5 (168 fractures) and W504 (172 fractures), which have similar fracture numbers, Well W504 has a higher slip tendency coefficient and better productivity. In Well W504, 84 fractures have a slip tendency coefficient greater than 0.25, accounting for 48.8%; in Well W5, 55 fractures have a slip tendency coefficient greater than 0.25, accounting for 32.7%. This indicated that when the number of fractures is similar, wells with more effective fractures presented better productivity, further demonstrating that fracture mechanical effectiveness imposed a strong control on productivity in the F_I17 strike-slip fault zone.

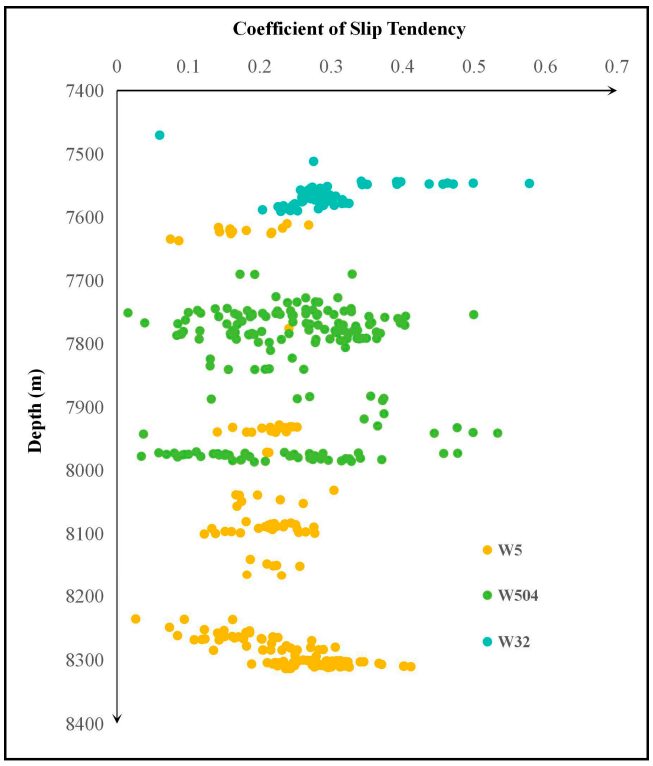


Figure 19. The relationship between slip tendency coefficient, dilation tendency coefficient, leakage factor, and pressure drop and production rate.

5.5. Application of Fracture Mechanical Effectiveness in Development

In ultra-deep carbonate reservoirs, fractures around the wellbore affect the development scheme by controlling fluid flow. Wells in the F_I17 strike-slip fault zone mainly produce via a natural flow at the initial development stage. As the formation pressure gradually declines, the mechanical effectiveness of fractures decreases, which in turn leads to productivity reduction. When the pressure drops to the fracture closure pressure, the well may cease flowing. To improve productivity, water or gas injection can be adopted for energy supplementation after a certain period of production. The increase in formation pressure can gradually raise the proportion of effective fractures, thereby restoring productivity (Figure 7). However, if secondary development causes excessively high formation pressure and fractures reach their opening pressure, the overly opened fractures can be prone to water channeling. Therefore, reasonable control of formation pressure is a necessary procedure for the development of ultra-deep carbonate reservoirs.

Combined with Equations (14)–(18), the fracture opening pressure and closure pressure of the five wells were obtained (Figure 15). Taking Well W32 as an example, the fracture opening pressure ranged from 148 to 237 MPa, and the closure pressure ranged from 18 to 59 MPa. Well W32 had been produced by depletion development in the early stage. When the formation pressure dropped to 31.2 MPa, the well stopped flowing. At this moment, 87.6% of the fractures had reached their closure pressure, and most fractures were closed and became ineffective. In the later stage, when converting fractures into effective fractures through secondary development measures such as water injection, the fracture opening pressure should be emphasized to avoid water channeling. However, not all fractures can be reopened by replenishing formation energy. The opening pressure of some fractures exceeded 180 MPa, which was beyond the upper limit of engineering pressure.

Well W32 was developed in the early stage, and depletion-driven production caused excessive formation pressure decline. Referring to fracture stress-sensitivity experiments, fractures exhibited significant stress-sensitivity damage (Table 3). During the process

where the effective confining pressure increased and then decreased, the gas permeability of the fractured core sample recovered to less than 40% (Figure 20). This indicated that fluid flow dominated by fractures may not be restored to the initial development level via pressure replenishment after excessive formation pressure decline. Therefore, cyclic injection–production was recommended to minimize the fluctuation range of formation pressure as much as possible.

Table 3. Stress sensitivity data of fractures.

Effective Confining Pressure (MPa)		Permeability (mD)	Permeability Damage Rate (%)	Permeability Ratio (%)
process of increasing effective confining pressure	2.5	0.006497	0	100
	3.5	0.005011	22.88	77.12
	5	0.003556	45.27	54.73
	7	0.002349	63.85	36.15
	9	0.00173	73.37	26.63
	11	0.001338	79.4	20.6
	15	0.00082	87.38	12.62
	20	0.000411	93.68	6.32
process of decreasing effective confining pressure	20	0.000411	93.68	6.32
	15	0.000504	92.24	7.76
	11	0.000595	90.85	9.15
	9	0.000695	89.31	10.69
	7	0.00084	87.08	12.92
	5	0.00113	82.61	17.39
	3.5	0.001567	75.88	24.12
	2.5	0.00202	68.91	31.09

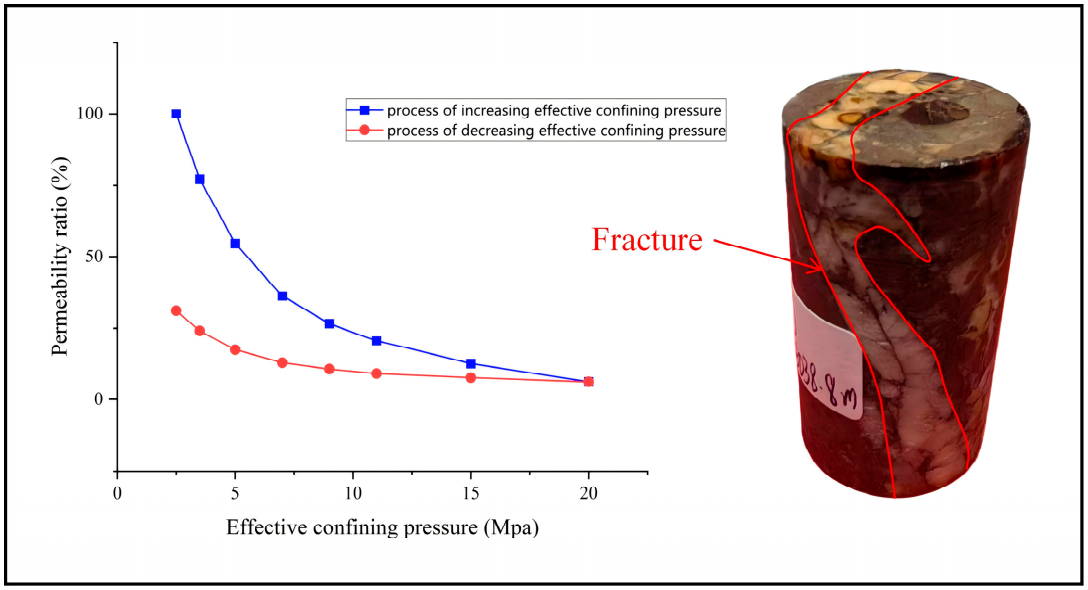


Figure 20. Stress sensitivity experiment of fractures.

5.6. Limitations and Future Prospects

The fracture effectiveness evaluation workflow developed in this study has been applied to a certain extent in the F_I17 strike-slip fault zone of the Fuman Oilfield. However, this method primarily focused on the evaluation of individual fractures or single-type fracture systems. In fact, fracture network connectivity was also one of the critical factors governing the control of fractures over fluid flow. Fracture networks formed by the interconnection of individual fractures served as the primary pathways for fluid communication, whereas isolated fractures—especially those with small scales—barely contributed to fluid flow. Therefore, future research in this area will adopt topological methods, which are currently widely used in the quantitative evaluation of connectivity, to further supplement the investigation of fracture network connectivity (Figure 21). Based on the connection

nodes and branches of different connection types within fracture networks [44], topological methods can employ statistical approaches to calculate various topological parameters that characterize connectivity, thereby improving the understanding of how fractures in ultra-deep marine carbonate reservoirs control fluid seepage.

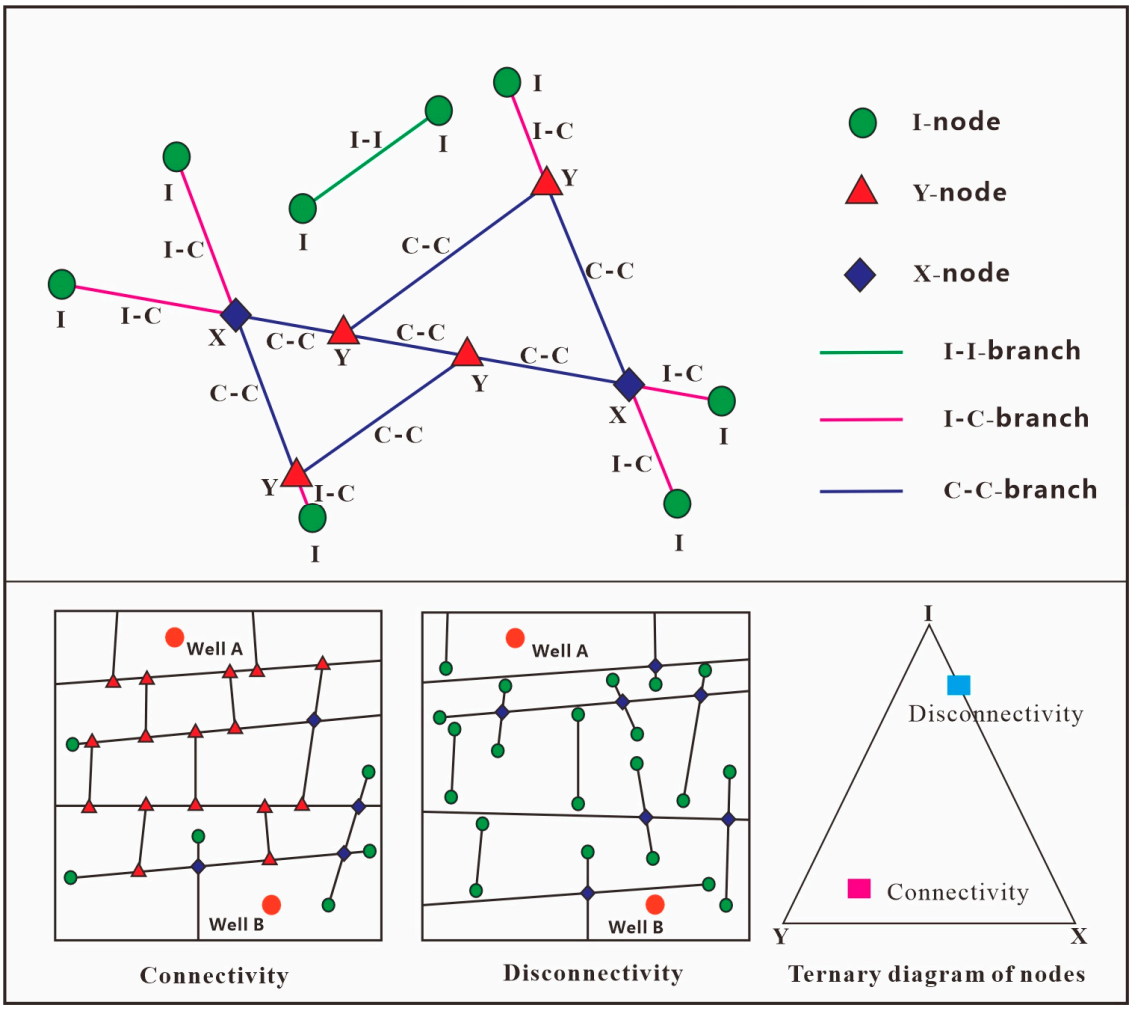


Figure 21. Schematic diagram of quantitative evaluation of fracture network connectivity by topological method.

6. Conclusions

This study proposed an integrated geological and geomechanical method for investigating the fracture effectiveness of ultra-deep carbonate reservoirs in the F_I17 strike-slip fault zone, and provided references for exploration deployment and development schemes from the perspective of fracture effectiveness.

(1) Fractures can serve as crucial seepage channels in the carbonate reservoirs of the F_I17 strike-slip fault zone in the Fuman Oilfield. Through core analysis, thin-section observation, and imaging logging, at least three phases of structural fractures have been identified, among which high-angle to near-vertical fractures are the most well-developed, striking obliquely at a small angle to the main fault. Fluid inclusion thermometry indicates that the fractures have undergone at least three phases of calcite cementation, where early fractures were severely filled, while late-stage fractures exhibited good effectiveness.

(2) A large number of stylolites were developed in ultra-deep carbonate rocks and were currently completely filled with asphaltenes. Dense horizontal zigzag stylolites can cut through early fractures, thereby reducing the overall effectiveness of the fractures.
(3) Mechanical effectiveness evaluation of multi-scale fractures in the F_I17 strike-slip fault zone was conducted using slip tendency as the primary criterion, supplemented by dilation tendency and leakage factor. Fractures characterized by high slip tendency, high leakage factor, and moderate dilation tendency were considered to possibly have better effectiveness in the study area. It provided a useful exploration for the correlation between mechanical effectiveness and productivity.
(4) The calculation of fracture opening pressure and closure pressure was used to define a reasonable formation pressure interval for secondary development. It is recommended to narrow the fluctuation range of formation pressure and adopt cyclic injection–production.
(5) In addition to data limitations in current fracture effectiveness evaluations, there was insufficient understanding of the fracture network connectivity in terms of methodology. In the future, topological methods and other approaches should be adopted to quantitatively evaluate fracture network connectivity, so as to improve the research on fracture effectiveness in ultra-deep carbonate reservoirs.

Author Contributions: Conceptualization, K.W. (Kongyou Wu) and Z.L.; methodology, B.W. and Z.L.; software, Z.L.; validation, H.Z. and K.X.; formal analysis, B.W. and K.X.; investigation, K.W. (Kehao Wang) and Z.L.; resources, K.W. (Kongyou Wu); data curation, B.W. and H.Z.; writing—original draft preparation, Z.L.; writing—review and editing, B.W.; visualization, Z.L.; supervision, K.W. (Kongyou Wu) and H.Z.; project administration, K.W. (Kongyou Wu); funding acquisition, K.W. (Kongyou Wu). All authors have read and agreed to the published version of the manuscript.

Funding: This work was supported by the National Natural Science Foundation of China (Grant No. 42272155) and the Major Science and Technology Special Program of Xinjiang Uygur Autonomous Region (Grant No. 2024A01010).

Institutional Review Board Statement: Not applicable.

Informed Consent Statement: Not applicable.

Data Availability Statement: The data supporting the conclusions of this study can be obtained from the corresponding authors.

Acknowledgments: The authors would like to thank PetroChina Tarim Oilfield Company for providing the data essential for this study and for the support throughout the research process. The authors also thank the reviewers and editors for their professional reviews and constructive comments.

Conflicts of Interest: Authors Hui Zhang and Ke Xu were employed by the company PetroChina Tarim Oilfield. The remaining authors declare that the research was conducted in the absence of any commercial or financial relationships that could be construed as a potential conflict of interest.

References

1. Laubach, S.; Zeng, L.; Hooker, J.; Wang, Q.; Zhang, R.; Wang, J.; Ren, B. Deep and ultra-deep basin brittle deformation with focus on China. *J. Struct. Geol.* **2023**, *175*, 104938. [CrossRef]
2. Shi, J.; Zhao, X.; Pan, R.; Zeng, L.; Luo, W. Natural fractures in the deep Sinian marine carbonates of the central Sichuan Basin, China: Implications for reservoir quality. *J. Pet. Sci. Eng.* **2022**, *216*, 110829. [CrossRef]
3. Lu, Z.; Ping, H.; Chen, H.; Zhang, Y.; Xie, Z.; Zhang, Y.; Chen, Z.; Yang, X.; Zhang, X.; Yang, K.; et al. Geochemical Characteristics of Ordovician Crude Oils in the F_I17 Strike-Slip Fault Zone of the Fuman Oilfield, Tarim Basin: Implications for Ultra-Deep Hydrocarbon Accumulation in the Tarim Basin. *Mar. Pet. Geol.* **2024**, *163*, 106800. [CrossRef]
4. Guo, Y.; Liang, Y.; Li, J.; Gong, B. A novel connectivity-based hierarchical model for multi-scale fracture system in marine carbonate reservoir simulation. *Fuel* **2019**, *250*, 327–338. [CrossRef]
5. Caine, J.; Evans, J.; Forster, C. Fault zone architecture and permeability structure. *Geology* **1996**, *24*, 1025–1028. [CrossRef]

6. Savage, H.; Brodsky, E. Collateral damage: Evolution with displacement of fracture distribution and secondary fault strands in fault damage zones. *J. Geophys. Res.* **2011**, *116*, B03405. [CrossRef]
7. Zeng, L.; Song, Y.; Liu, G.; Tan, X.; Xu, X.; Yao, Y.; Mao, Z. Natural fractures in ultra-deep reservoirs of China: A review. *J. Struct. Geol.* **2023**, *175*, 104954. [CrossRef]
8. Liu, J.; Ding, W.; Dai, J.; Gu, Y.; Yang, H.; Sun, B. Quantitative multiparameter prediction of fault-related fractures: A case study of the second member of the Funing Formation in the Jinhu Sag, Subei Basin. *Pet. Sci.* **2018**, *15*, 468–483. [CrossRef]
9. Xu, K.; Yang, H.; Zhang, H.; Ju, W.; Li, C.; Fang, L.; Wang, Z.; Wang, H.; Yuan, F.; Zhao, B.; et al. Fracture effectiveness evaluation in ultra-deep reservoirs based on geomechanical method, Kuqa Depression, Tarim Basin, NW China. *J. Pet. Sci. Eng.* **2022**, *215*, 110604. [CrossRef]
10. Li, H.; Wang, Q.; Qin, Q.; Ge, X. Characteristics of natural fractures in an ultradeep marine carbonate gas reservoir and their impact on the reservoir: A case study of the Maokou Formation of the JLS Structure in the Sichuan Basin, China. *Energy Fuels* **2021**, *35*, 16933. [CrossRef]
11. Pan, B.; Yuan, M.; Fang, C.; Liu, W.; Guo, Y.; Zhang, L. Experiments on acoustic measurement of fractured rocks and application of acoustic logging data to evaluation of fractures. *Pet. Sci.* **2017**, *14*, 520–528. [CrossRef]
12. Forstner, S.; Laubach, S. Scale-dependent fracture networks. *J. Struct. Geol.* **2022**, *165*, 104748. [CrossRef]
13. Gong, L.; Wang, J.; Gao, S.; Fu, X.; Liu, B.; Miao, F.; Zhou, X.; Meng, Q. Characterization, controlling factors and evolution of fracture effectiveness in shale oil reservoirs. *J. Pet. Sci. Eng.* **2021**, *203*, 108655. [CrossRef]
14. Zhang, R.; Wang, K.; Zeng, Q.; Yu, C.; Wang, J. Effectiveness and petroleum geological significance of tectonic fractures in the ultra-deep zone of the Kuqa foreland thrust belt: A case study of the Cretaceous Bashijiqike Formation in the Keshen gas field. *Pet. Sci.* **2021**, *18*, 728–741. [CrossRef]
15. Wang, Z.; Xu, K.; Zhang, H.; Wang, H.; Yin, G.; Wang, Z.; Zhao, W. Fracture effectiveness evaluation of ultra-deep tight sandstone reservoirs: A case study of the Keshen gas field, Tarim Basin, West China. *Front. Earth Sci.* **2022**, *10*, 883479. [CrossRef]
16. Xu, X.; Zeng, L.; Dong, S.; Diwu, P.; Li, H.; Liu, J.; Han, G.; Xu, H.; Ji, C. Fracture Effectiveness and Its Influence on Gas Productivity in Ultra-Deep Tight Sandstone Reservoirs of the Keshen Gas Field, Tarim Basin. *Acta Geol. Sin.* **2024**, *98*, 1557–1573. [CrossRef]
17. Xu, K.; Cai, Z.; Zhang, H.; Yin, G.; Wang, Z.; Fang, L.; Wang, H.; Qian, Z.; Zhang, W.; Lai, S.; et al. Geomechanical Modeling of Ultradeep Fault-Controlled Carbonate Reservoirs and Its Application: A Case of the Fuman Oilfield in Tarim Basin. *Energy Sci. Eng.* **2023**, *11*, 3332–3343. [CrossRef]
18. Yu, J.; Shi, K.; Wang, Q.; Liu, B.; Han, J.; Song, Y.; Kong, Y.; Jiang, W. Structural Diagenesis of Deep Carbonate Rocks Controlled by Intra-Cratonic Strike-Slip Faulting: An Example in the Shunbei Area of the Tarim Basin, NW China. *Basin Res.* **2022**, *34*, 1601–1631. [CrossRef]
19. Toussaint, R.; Aharonov, E.; Koehn, D.; Gratier, J.P.; Ebner, M.; Baud, P.; Rolland, A.; Renard, F. Stylolites: A Review. *J. Struct. Geol.* **2018**, *114*, 163–195. [CrossRef]
20. Yin, G.; Wu, K.; Ju, W.; Qin, Y.; Qian, Z.; Xu, K.; Lu, Z.; Wang, P.; Liang, X.; Liang, Y. In-situ stress prediction in ultra-deep marine carbonate reservoirs of Fuman Oilfield, Tarim Basin of China. *Front. Energy Res.* **2023**, *11*, 1271377. [CrossRef]
21. Tan, X.; Zhang, Y.; Lyu, W.; Xie, Z.; Zeng, L.; Yuan, J.; Xiong, T.; Song, Y.; Li, H.; Zhang, K. A study on the variability in the distribution of fracture networks in typical segments of ultra-deep strike-slip faults-A case study of the $F_1$17 fault in the Fuman area, Tarim Basin. *Geol. Rev.* **2025**, *71*, 1403–1413. (In Chinese) [CrossRef]
22. Wang, Q.; Yang, H.; Li, Y.; Lv, X.; Zhang, Y.; Zhang, Y.; Sun, C.; Ouyang, S. Control of strike-slip fault on the large marine carbonate reservoir in Fuman, Tarim Basin-a reservoir model. *Earth Sci. Front.* **2022**, *29*, 239–251. (In Chinese) [CrossRef]
23. Qiao, J.; Chang, S.; Zeng, J.; Cao, P.; Dong, K.; Wang, M.; Yang, J.; Liu, Y.; Long, H.; An, T.; et al. Origin of differential hydrocarbon accumulation in ultra-deep marine carbonate reservoirs along strike-slip fault zones in the Fuman area, northern Tarim Basin. *Oil Gas Geol.* **2024**, *45*, 226–1246. (In Chinese) [CrossRef]
24. Deng, X.; Chang, S.; Chen, F.; Chen, G.; Wang, P.; Cao, P.; Wang, M.; Yao, Q.; Zhao, L.; Ye, T. Geological characteristics and implications of ultra-deep fractured breccia reservoirs in the Fuman Oilfield, Tarim Basin. *Mar. Orig. Pet. Geol.* **2025**, *30*, 228–238. (In Chinese) [CrossRef]
25. Wang, Q.; Yang, H.; Wang, R.; Li, S.; Deng, X.; Li, Y.; Chang, L.; Wan, X.; Zhang, Y. Discovery and exploration technology of fault-controlled large oil and gas fields of ultra-deep formation in strike slip fault zone in Tarim Basin. *China Pet. Explor.* **2021**, *26*, 58–71. (In Chinese) [CrossRef]
26. Deng, X.; Chang, S.; Liu, Z.; Wang, M.; Chen, J.; Du, Y. Concept, geological model and seismic characterization of ultra-deep fault-fracture bodies. *Oil Geophys. Prospect.* **2024**, *59*, 1099–1110. (In Chinese) [CrossRef]
27. Cao, F.; He, J.; Deng, H.; Li, K.; Xie, X.; Wang, W.; Mao, J.; Sun, J. Evaluation of the effectiveness of tectonic fractures in shale reservoirs of Fengcheng Formation in Mabei area and its geological significance for oil and gas. *J. China Univ. Min. Technol.* **2024**, *53*, 1198–1217. (In Chinese) [CrossRef]

28. Bowers, G. Pore Pressure Estimation From Velocity Data: Accounting for Overpressure Mechanisms Besides Undercompaction. *SPE Drill. Comp.* **1995**, *10*, 89–95. [CrossRef]
29. Liu, J.; Huang, C.; Zhou, L.; Chen, Q.; Zhang, S. Estimation of the rock mechanics and in-situ stress parameters of carbonate reservoirs using array soniclogging: A case study of Shunbei No.4 block. *J. Geomech.* **2024**, *30*, 394–407. (In Chinese) [CrossRef]
30. Wang, K.; Dai, J. A Quantitative Relationship Between the Crustal Stress and Fault Sealing Ability. *Acta Pet. Sin.* **2012**, *33*, 74–81. (In Chinese) [CrossRef]
31. Barton, C.; Zoback, M.; Moos, D. Fluid flow along potentially active faults in crystalline rock. *Geology* **1995**, *23*, 683–686. [CrossRef]
32. Zoback, M.; Peska, P. In-situ stress and rock strength in the GBRN/DOE Pathfinder Well, South Eugene Island, Gulf of Mexico. *J. Pet. Technol.* **1995**, *47*, 582–585. [CrossRef]
33. Morris, A.; Ferrill, D.; Henderson, D. Slip-tendency analysis and fault reactivation. *Geology* **1996**, *24*, 275–278. [CrossRef]
34. Byerlee, J.; Mjachkin, V.; Summers, R.; Voevoda, O. Structures Developed in Fault Gouge during Stable Sliding and Stick-Slip. *Tectonophysics* **1978**, *44*, 161–171. [CrossRef]
35. Zoback, M.D. *Reservoir Geomechanics*; Cambridge University Press: Cambridge, UK, 2007.
36. Kulikowski, D.; Amrouch, K.; Cooke, D.; Gray, M. Basement Structural Architecture and Hydrocarbon Conduit Potential of Polygonal Faults in the Cooper-Eromanga Basin, Australia. *Geophys. Prospect.* **2018**, *66*, 366–396. [CrossRef]
37. Liu, J.; Ding, W.; Gu, Y.; Xiao, Z.; Dai, J.; Dai, P.; Chen, X.; Zhao, G. Methodology for predicting reservoir breakdown pressure and fracture opening pressure in low-permeability reservoirs based on an in situ stress simulation. *Eng. Geol.* **2018**, *246*, 222–232. [CrossRef]
38. Tian, Y.; Chen, Q.; Wu, J.; Li, K.; Yan, C.; He, Y. Determination of the fracture closure pressure in fractural-cavity marine carbonate reservoirs using a failure criterion based on asperity behavior. *Front. Earth Sci.* **2024**, *12*, 1518370. [CrossRef]
39. Li, Y.; Ru, Z.; Deng, S.; Lin, H.; Han, J.; Zhang, J.; Huang, C. Experimental Evaluation and Hydrocarbon Significance of Natural Fractures in Shunbei Ultra-Deep Carbonate Reservoir, Tarim Basin. *Pet. Geol. Exp.* **2023**, *45*, 422–433. [CrossRef]
40. Zeng, L.; Song, Y.; Han, J.; Han, J.; Yao, Y.; Huang, C.; Zhang, Y.; Tan, X.; Li, H. Control of structure and fluid on ultra-deep fault-controlled marine carbonate fracture-vug reservoirs in Tarim Basin, NW China. *Pet. Explor. Dev.* **2018**, *52*, 128–139. (In Chinese) [CrossRef]
41. Ni, C.; Hu, A.; Jin, T.; Duan, J.; Qiao, Z.; Chang, S.; Huang, Y.; Shen, A.; Chen, H. Application of new dating and temperature-measuring technologies in study of strike-slip fault-controlled reservoirs and hydrocarbon accumulation: A case study of Ordovician strata in non-foreland area of Tarim Basin, NW China. *Pet. Explor. Dev.* **2025**, *52*, 1328–1340. (In Chinese) [CrossRef]
42. Yao, C.; Qiao, Z.; Luo, X.; Zhang, T.; Li, B.; Chang, S.; Zhang, Z.; Chen, J. Stages and Evolution of Strike-Slip Faults of the Ultra-Deep-Burial Ordovician Strata in Fuman Oilfield, Tarim Basin: Evidence from U-Pb Geochronology of Siliceous Minerals. *Minerals* **2025**, *15*, 270. [CrossRef]
43. Ferrill, D.; Morris, A.; McGinnis, R.; Smart, K.; Wigginton, S.; Hill, N. Mechanical stratigraphy and normal faulting. *J. Struct. Geol.* **2017**, *94*, 275–302. [CrossRef]
44. Sanderson, D.; Nixon, C. The use of topology in fracture network characterization. *J. Struct. Geol.* **2015**, *72*, 55–66. [CrossRef]

Disclaimer/Publisher's Note: The statements, opinions and data contained in all publications are solely those of the individual author(s) and contributor(s) and not of MDPI and/or the editor(s). MDPI and/or the editor(s) disclaim responsibility for any injury to people or property resulting from any ideas, methods, instructions or products referred to in the content.